drones

MDPI

Article

Advancing mmWave Altimetry for Unmanned Aerial Systems: A Signal Processing Framework for Optimized Waveform Design

Maaz Ali Awan [1], Yaser Dalveren [2], Ali Kara [3] and Mohammad Derawi [4,*]

[1] Graduate School of Natural and Applied Sciences, Department of Electrical and Electronics Engineering, Atilim University, Ankara 06830, Turkey; awan.maaz@student.atilim.edu.tr
[2] Department of Electrical and Electronics Engineering, Izmir Bakircay University, Izmir 35665, Turkey; yaser.dalveren@bakircay.edu.tr
[3] Department of Electrical and Electronics Engineering, Gazi University, Ankara 06570, Turkey; akara@gazi.edu.tr
[4] Department of Electronic Systems, Norwegian University of Science and Technology, 2815 Gjovik, Norway
* Correspondence: mohammad.derawi@ntnu.no

Abstract: This research advances millimeter-wave (mmWave) altimetry for unmanned aerial systems (UASs) by optimizing performance metrics within the constraints of inexpensive automotive radars. Leveraging the software-defined architecture, this study encompasses the intricacies of frequency modulated continuous waveform (FMCW) design for three distinct stages of UAS flight: cruise, landing approach, and touchdown within a signal processing framework. Angle of arrival (AoA) estimation, traditionally employed in terrain mapping applications, is largely unexplored for UAS radar altimeters (RAs). Time-division multiplexing multiple input–multiple output (TDM-MIMO) is an efficient method for enhancing angular resolution without compromising the size, weight, and power (SWaP) characteristics. Accordingly, this work argues the potential of AoA estimation using TDM-MIMO to augment situational awareness in challenging landing scenarios. To this end, two corner cases comprising landing a small-sized drone on a platform in the middle of a water body are included. Likewise, for the touchdown stage, an improvised rendition of zoom fast Fourier transform (ZFFT) is investigated to achieve millimeter (mm)-level range accuracy. Aptly, it is proposed that a mm-level accurate RA may be exploited as a software redundancy for the critical weight-on-wheels (WoW) system in fixed-wing commercial UASs. Each stage is simulated as a radar scenario using the specifications of automotive radar operating in the 77–81 GHz band to optimize waveform design, setting the stage for field verification. This article addresses challenges arising from radial velocity due to UAS descent rates and terrain variation through theoretical and mathematical approaches for characterization and mandatory compensation. While constant false alarm rate (CFAR) algorithms have been reported for ground detection, a comparison of their variants within the scope UAS altimetry is limited. This study appraises popular CFAR variants to achieve optimized ground detection performance. The authors advocate for dedicated minimum operational performance standards (MOPS) for UAS RAs. Lastly, this body of work identifies potential challenges, proposes solutions, and outlines future research directions.

Keywords: mmWave; TDM-MIMO; altimetry; UAS; FMCW; CFAR; ZFFT; WoW

Citation: Awan, M.A.; Dalveren, Y.; Kara, A.; Derawi, M. Advancing mmWave Altimetry for Unmanned Aerial Systems: A Signal Processing Framework for Optimized Waveform Design. *Drones* **2024**, *8*, 440. https://doi.org/10.3390/drones8090440

Academic Editors: Chao Huang, Yan Wang, Zhaojian Li, Henglai Wei and Zhongxu Hu

Received: 9 July 2024
Revised: 15 August 2024
Accepted: 27 August 2024
Published: 28 August 2024

1. Introduction

Unfazed by the inherent constraints of light and barometric altitude sensors, radars employ EM waves as an optimal means to attain precise altitude information during the autonomous landing stage of UASs [1]. Amongst the radar waveforms capable of measuring altitude, pulse Doppler radars, with their low-duty cycle, are limited by higher peak power demand, raising concerns from a public health standpoint [2]. Additionally, the inherent rapid switching requirement impedes the measurement of the very low altitudes necessary in the touchdown stage. Conversely, the simultaneous transmission and reception in

FMCW radars make them more suitable for a dynamic range of altitude requirements [3]. Over the past three decades, mmWave automotive radars have advanced significantly, incorporating compact, highly flexible, and cost-effective 45 nm chipsets that integrate control, signal processing, and RFFE. The maturation of these platforms, coupled with researchers' yearning for exploration, has expanded potential use cases beyond the automotive realm. The current landscape of widespread 5G communication network deployment has led to interference with universally allocated bands for RAs [4]. Aptly, mmWave bands, particularly 77 GHz, hold considerable potential as a feasible avenue for migrating RAs in commercial aviation and a broad range of UASs.

This article is a continuation of ongoing work with an initial investigation covering theoretical and mathematical discourse concerning the potential use of mmWave automotive radars for UAS altimetry [5]. In commercial aviation, MOPS serve as a reference for RA development [6,7]. The focal point of the preceding article was to align the MOPS for RAs in commercial aviation with the operational requirements of UASs. In the absence of dedicated MOPS for UASs, an adaptation from existing standards for commercial aviation was a reasonable compromise given the largely similar requirements, particularly in the landing stage. This required a systematic approach, starting with the fundamentals of FMCW radars and then delving into the complexities of performance metrics due to their interconnectedness. The rationale for choosing an automotive radar was based on commercial availability and cost-effectiveness in the mmWave band. This selection was further motivated by the promising SWaP characteristics. Moreover, the maturity of said technology was appraised with a state-of-the-art review. A compelling case for the exploration of automotive radars beyond their conventional domain was supported by comparative works. Lastly, detailed explanations for deriving waveform specifications from the operational requirements were furnished using a realistic test case.

The process of altitude measurement in UASs using FMCW radars can be categorized into two main domains. The first involves the generation of the waveform by the radar sensor in alignment with the operational requirements of the UAS. The second concerns the signal processing stage, where the waveform is converted into usable altitude data. Given the scarcity of reference literature and the novel nature of mmWave altimetry, a comprehensive and simplified discussion was essential to establish both feasibility and a foundation for this new direction. With this in mind, a detailed discussion covering state-of-the-art developments, the adaptation of MOPS for UASs, and the theoretical framework for performance metrics was provided in the previous article. Therefore, it was deemed necessary to dedicate this article specifically to the signal processing domain.

This study provides a seamless extension of the preceding work, with the framework for waveform design following accordingly. While the MOPS for commercial aviation are a good reference, there are no restrictions to stretching the performance metrics even further. These improvements are poised to serve a wide range of existing and future requirements of UASs. Furthermore, there is tremendous potential for capability enhancement. Fittingly, this work encompasses three unique stages of UAS flight: cruise, landing approach, and touchdown. The ensuing sections rationalize the unique operational requirements for each stage followed by derivation of resultant waveform specifications from a theoretical and mathematical standpoint. The premise of defining these stages is to exhibit the versatility of an adaptive waveform designed to cater to a dynamic range of operational requirements. The cruise stage is inferred from the previous work, with the addition of signal processing aspects. The term "cruise" refers to the normal flight operation of a drone while it is carrying out its intended task. This stage does not entail landing and the goal is to maintain constant altitude AGL in surveillance applications [8]. Appropriately, high altitude estimation coupled with the finest possible range resolution is targeted for this stage.

RAs are most commonly utilized in aviation during the landing approach [9]. In the existing landscape of industrial expansion, there is a growing trend toward the deployment of small-sized UASs in a plethora of applications, including agriculture [10], law enforcement [11], and traffic management [12]. At the same time, the safety of these UASs

is equally critical, particularly during the autonomous landing. Conventional RAs having a single Tx and Rx antenna pair with a wide HPBW lack the spatial information necessary for estimating true altitude along the radar boresight directly under the airframe. For instance, a highly reflective off-boresight object may cause an inaccurate altitude measurement [13]. In light of this limitation, it is proposed that the AoA may be leveraged for the estimation of true altitude. It is envisaged that the addition of this capability will augment situational awareness significantly and improve the overall safety standards for autonomous landing of UASs. To this end, a landing scenario comprising a VTOL drone on a ship in a water body is simulated. The aim is to augment other onboard sensors during the landing stage.

WoW systems in aircraft are used to estimate the instant when its weight starts to rest on its wheels. In the context of fixed-wing commercial UASs, such a system informs the FCC that the aircraft has safely landed, and necessary control processes are engaged accordingly [14]. By providing mm-accuracy altitude with a high level of confidence, the RA can serve as a reliable backup to the WoW system in UASs.

Primarily, considering the operational advantages of enhanced range accuracy and precise altitude estimation, the primary objective of this research endeavor is to develop an adaptive waveform. Consequently, it is imperative to elucidate in sufficient detail the signal-processing aspects related to the estimation of high altitude, AoA, and high accuracy during the three stages of flight, all within the constraints imposed by the hardware of automotive radars.

The software-defined architecture of automotive radar chosen for this endeavor allows for the realization of the intended objective. However, rationalization of operational requirements is mandatory to avoid setting too ambitious benchmarks. The solution lies in prioritizing the relevant performance metric for the respective flight stage while balancing the other metrics with reasonable trade-offs. For instance, the cruise stage does not necessitate a quick update rate and fine range resolution, but it requires a higher altitude. Similarly, during the landing stage, update rate and range resolution take precedence over high altitude. Lastly, the touchdown stage necessitates the highest possible update rate and range resolution with a very lenient altitude requirement. From an SWaP standpoint, a single radar capable of adaptively switching waveforms aligns well with the objective of improving operational endurance on a wide range of UASs.

To achieve the said objectives, legacy and contemporary signal processing techniques in the literature were reviewed. Each stage of the flight was treated as a radar scenario and simulated using the radar toolbox in MATLAB [15]. The simulation environment provided plentiful options for generating FMCW waveforms as well as propagation configurations using phased array antennae. Typically, the task of propagating FMCW waveforms in the radar LoS and acquiring signals through ADC is performed in hardware. Subsequently, ADC samples are transferred to simulation software for post-processing. Administratively, this approach is inefficient, as emulating multiple scenarios for each flight stage consumes significant time, energy, and resources. To address this, the study presented in [16] integrated the entire process into the simulation software, utilizing the hardware specifications of the commercial radar platform, IWR1843, operating within the 77–81 GHz frequency band. This method optimized the waveform design process while significantly conserving resources. Afterward, range profiles were subject to CFAR detection for altitude reporting. However, the touchdown stage, employing the ZFFT algorithm, was implemented directly on the radar due to the relative ease of emulating the target, the runway surface. The radar was mounted on a tripod stand and positioned against a flat concrete wall to simulate the runway surface at close range.

TDM-MIMO radars have been prevalent in automotive applications for a while now [17]. They utilize the concept of virtual antennas to estimate the AoA of the target in the radar FOV. Conventionally, fast-time and slow-time matrices are used for detecting targets in range and Doppler bins. The use of multiple virtual antennas extends these matrices in the third dimension to form radar cubes [18]. Signal processing techniques are then applied to these radar cubes to simultaneously estimate the range, velocity, and AoA.

Within the scope of the proposed adaptive mmWave FMCW waveform for UAS altimetry, all three aspects are important. Most conventional RAs provide range information only [19]. Academic discussions on the use of radar cubes in radar applications are largely uncharted in the literature.

The radial velocity resulting from the ROD and variations in terrain profile present a substantial difficulty that must be carefully considered during the waveform design process. Fittingly, explanations in theory and mathematics are provided for characterization and subsequent compensation. Until now, a detailed discussion on this topic has been lacking. The following sections demonstrate that, in the absence of a direct requirement to estimate the ROD, the resultant radial velocity component does not influence altitude measurement despite variations in terrain profile. Moreover, when properly accounted for, it does not impact the AoA, even with the application of TDM-MIMO.

Three widely utilized variants of CFAR employ specific parameters to balance sensitivity and the probability of false alarms [20]. Hence, it was imperative to discuss the selection of an appropriate CFAR variant tailored to the requirements of each flight stage. This study seeks to address this gap by evaluating popular CFAR variants to optimize detection performance for ground surfaces.

The use of mmWave automotive radars has been reported for mm-level accuracy in liquid-level sensing [21]. Traditionally, ZFFT has been used for the conservation of resources by targeting a specific portion of interest from the available spectrum. Legacy approaches aim to achieve the same spectral resolution while significantly reducing the order of FFT. Although used in mm-level accurate sensing of liquids, ZFFT for UAS altimetry has not been investigated. Contrary to the conventional approach, the objective is to target a small portion of the spectrum and perform a high-order FFT for increased spectral resolution. Consequently, very high accuracy can be leveraged for the estimation of touchdown instant as a software redundancy in the WoW system of UASs. In this work, the specifics of ZFFT are appraised for potential use in the intended application. A description of the improvised algorithm with a methodology for efficient implementation is furnished, considering the constraints of radar hardware. A coarse altitude estimation method is provided for identifying the ROI. The mathematical expressions and theoretical aspects of cited concepts may seem daunting to readers new to this field or from other backgrounds. To address this concern and in continuation with the tone of the previous article, a tutorial theme is adopted. The entire discussion is broken down into fundamental and relatable concepts.

Thus, the main contributions of this body of work are the following:

- Signal processing flow in a radar cube for mmWave altimetry.
- Design of an adaptive FMCW waveform for varied operational requirements.
- Appraisal and compensation of radial velocity due to UAS ROD and terrain profile.
- Use of TDM-MIMO for situational awareness in autonomous landing of UASs.
- mmWave altimetry as a software redundancy for WoW systems using ZFFT.
- Simulation of radar scenarios using hardware specifications of a commercial radar platform, IWR1843, operating at 77 GHz.
- Characterization of CFAR variants for optimal detection performance.

The remainder of the article is structured as follows: Section 2 provides an overview of the reference literature. Section 3 summarizes the fundamental concepts and aspects common to the entirety of the article. To seamlessly bridge the discussion, an overview of methodology is provided in Section 4. The ensuing Section 5 covers the specifics of the cruise stage. Section 6 entails AoA estimation using TDM-MIMO for enhanced situational awareness. Section 7 summarizes the details of ZFFT for use in WoW systems during the touchdown stage. The authors' discussion, future research direction, and challenges are penned in Section 8. Finally, Section 9 concludes the article.

2. Reference Works

As a relatively nascent research area, the literature available that directly serves as a reference for mmWave altimetry is limited. Nevertheless, in line with the objectives of this work, the proposed solution and methodologies were deliberated after a thorough review of reference works. The ensuing subsections entail the reference works that established the foundation for this study.

2.1. Previous Work

The authors' previous work laid the groundwork for the in-depth exploration of signal processing aspects covered in this study. Interested readers are encouraged to refer to the previous work for a foundational understanding of mmWave altimetry for UAS using FMCW radars [5]. Nevertheless, for the sake of completeness, an abridged overview of relevant aspects is included. A crucial outcome of that study was the selection of the most suitable automotive radar for the intended application. Appropriately, the 77 GHz mmWave band was proposed as a viable avenue for the migration of existing RAs amidst 5G proliferation. After an exhaustive comparison, the Texas Instruments IWR1843 mmWave radar (Texas Instruments, Dallas, TX, USA) operating in the 77 GHz range stood out. Antenna configuration, complex baseband architecture, sampling rate, and computational prowess were important considerations in the decision-making process. The chosen device follows into this endeavor as well. Another important contribution of preliminary work was the estimation of ground clutter using hardware specifications of the radar platform in a pure look-down scenario. Eventually, a systems engineering approach was outlined for deriving waveform specifications from operational requirements. Insights into performance metric optimization were also provided, culminating in an adaptive waveform covered in this study.

2.2. Limitation of Conventional RAs

Legacy RAs for commercial aircraft are designed per the MOPS governed by aviation standards, EUROCAE ED-30 [6], and DO-155 [7]. The requirements specified in these standards have largely remained unadulterated for the last four decades. These rudimentary requirements are still well suited for the relatively easy landing scenarios in commercial aviation. As specified in the authors' previous work, dedicated MOPS of RAs do not exist for UASs. Accordingly, the existing aviation standards were adopted to initiate the discourse towards mmWave altimetry for UASs. The wide HPBW of the radar antenna is specified as a crucial metric in the existing MOPS. However, it signifies that EM waves are reflected off an elliptical projection with a very large area on the terrain. As highlighted in the introductory part, a strong reflection from a terrain patch at a high off-boresight position will entail an error in altitude measurement. Figure 1 shows the cross-sectional view of a terrain patch along the azimuthal plane of the radar antenna. There is uncertainty in altitude estimation; therefore, it is not possible to ascertain whether the height is R1, R2, or R3. Particularly, for small-sized VTOL drones relying on RA for landing on ships in the middle of a water body or a steep mountain slope, such errors may lead to detrimental outcomes. Similarly, in geological survey applications where a constant altitude AGL is mandatory over high-relief terrain, conventional RAs are likely to be error-prone. In light of the increasing deployment of UASs in a broad range of commercial applications, there is a burgeoning need to propel the discourse towards mmWave altimetry with the capability of AoA estimation.

2.3. Interferometric Radar Altimeters

Traditionally, IRAs with AoA estimation capability are employed in TRN systems and terrain mapping for remote sensing applications [22,23]. These systems aim to provide navigation aid to airborne systems in GPS-denied environments. Unlike a traditional RA offering only the range information, an IRA provides range, elevation, and azimuth information, thereby enhancing altitude accuracy. This work takes inspiration from the

concept of AoA estimation inherent in IRAs but takes a different tangent towards enhanced situational awareness for improved safety in the autonomous landing of UASs.

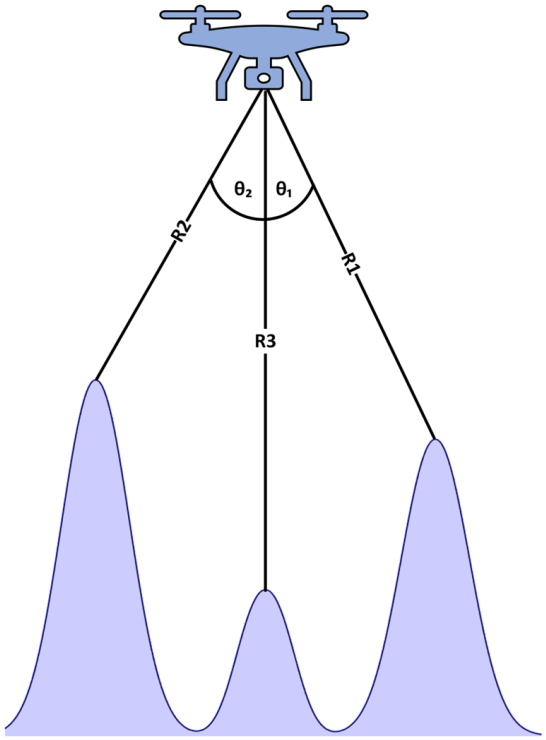

Figure 1. Uncertainty in altitude estimation due to wide HPBW of radar antenna [13].

2.4. TDM-MIMO for Automotive Applications

TDM-MIMO radars leverage virtual antennas to achieve increased angular resolution in AoA estimation, equivalent to a radar system with a significantly greater number of physical antennas [24]. Owing to favorable SWaP properties, it is employed in automotive safety applications for obstacle avoidance, pedestrian safety, and vehicle detection [25]. While state-of-the-art reviews offer valuable insights into industry trends and research directions, they often lack depth. Similarly, instructional materials from radar manufacturers, such as application notes, focus primarily on implementation considerations and offer only a rudimentary overview of theoretical concepts [26].

Nonetheless, all forms of the relevant literature and radar handbooks were consulted for this effort, and a comprehensive range of reference materials was incorporated. Given that this study focuses on signal processing, the literature on mmWave FMCW TDM-MIMO radar, notably the study in [27], serves as a valuable resource. This work employs a similar streamlined methodology within the framework of mmWave altimetry for UASs.

2.5. Legacy Use of CFAR

The CFAR algorithm has traditionally been used to detect targets in range-Doppler maps for automotive applications using mmWave FMCW radars [28]. The use of CFAR for ground surface detection has been reported in the literature [29]. However, the cited work lacks a mathematical foundation and does not explore performance aspects in depth. Another related study investigated the effectiveness of radar sensors in AGL altitude estimation but focused more on potential applications, providing limited depth [30]. The work most closely aligned with the altimetry use case utilized a 77 GHz mmWave FMCW radar chipset to measure the altitude of a small drone from the ground [31]. The cited study also employed a modified version of the CFAR algorithm for ground surface detection. There has been significant work characterizing the performance of various CFAR algorithm variants [32]. However, no comparative study has been conducted on their performance for

UAS altimetry in either simulation environments or practical experimentation. This paper aims to fill this gap by comparing various CFAR variants in a simulation environment. Additionally, it discusses the reasoning behind selecting the most appropriate variant to meet the specific needs of a particular flight stage.

2.6. Legacy Use of Zoom FFT

The legacy use of ZFFT aims to reduce the computational burden of FFT evaluation by targeting a band of interest, shifting it down to a DC component, and applying decimation. This process involves mixing, low-pass filtering, and downsampling to maintain spectral resolution while reducing computational complexity. ZFFT achieves the same spectral resolution by performing a smaller FFT on a decimated signal, providing an efficient alternative to the traditional FFT implementation [33]. In this work, contrary to its traditional use, ZFFT involves identifying the ROI followed by an additional layer of FFT, resulting in exceptionally high spectral resolution.

2.7. Reference Designs and Simulation Environment

As highlighted in the preliminary work, one of the reasons for selecting the Texas Instruments IWR1843 was the extensive literature, detailed reference designs, and community support available. Accordingly, implementation aspects related to windowing, FFT, radar cube generation, and CFAR detection were derived from the Texas Instruments mmWave SDK [34]. Additionally, details for the ZFFT algorithm were obtained from the high-accuracy sensing lab [21]. However, these references lack academic value. To address this gap, theoretical and mathematical insights are incorporated into the discussion in the subsequent sections. Radar scenarios were simulated using the Radar Toolbox in MATLAB [15], and the FMCW waveform was generated with the Phased Array System Toolbox [35]. It should be noted that all simulations were conducted using an LoS propagation model without considering reflections.

3. Preliminaries

This section addresses the fundamental concepts of FMCW radars and the signal processing aspects in contemporary systems. The concepts discussed are relevant to the waveform design process across all three flight stages of UASs. Thus, it is appropriate to consolidate this information to avoid repetition. The methodology for generating radar cubes, which includes time and frequency representations of data, is outlined as a preliminary step for subsequent CFAR detection and AoA estimation stages.

3.1. Overview of Performance Metrics

To facilitate convenient referencing throughout the article, performance metrics are consolidated in a single location for completeness. These metrics are fundamental mathematical expressions intrinsic to mmWave FMCW radar systems. While their derivation has been addressed in the preliminary work, a summary is provided in Table 1, which encompasses range, velocity, and AoA.

Table 1. Performance metrics in FMCW radars.

Range (m)	Velocity (m/s)	AoA (Radians)
$R = \frac{cf_{IF}}{2S}$	$V = \frac{\lambda \Delta f}{4\pi T_c}$	$\theta = \sin^{-1}\left(\frac{\lambda \Delta f}{2\pi d}\right)$
$\Delta R = \frac{c}{2B}$	$\Delta V = \frac{\lambda}{2T_f}$	$\Delta\theta = \frac{2}{N_{Rx}}$
$R_{max} = \frac{cf_s}{2S}$	$V_{max} = \frac{\lambda}{4T_c}$	$\theta_{max} = \sin^{-1}\left(\frac{\lambda}{2d}\right)$

where R, ΔR, and R_{max} are the range, range resolution, and maximum measurable range. V, ΔV, and V_{max} are the velocity, velocity resolution, and maximum measurable velocity. θ, $\Delta\theta$, and θ_{max} are the AoA, angular resolution, and maximum measurable AoA. c is the speed of light, f_{IF} is the intermediate frequency, S is the slope of FMCW chirp, and λ is the wavelength. Δf is the frequency shift, T_c is the duration of a single FMCW chirp, d is the antenna spacing, B is chirp BW, T_f is the duration of the chirp frame, N_{Rx} is the number of receive antennae, and f_s is the sampling frequency.

3.2. Point Cloud Generation in Automotive Radars

In line with the research objective, this study maximizes the utility of existing hardware and software components used in contemporary automotive radars, extending their application to mmWave altimetry for UASs. Point cloud generation serves as a suitable starting point, building the foundation for subsequent discussions. A point cloud is a collection of data points representing the spatiality and kinetics of detected objects within the radar field of view. Derived from range, velocity, and angular measurements, it provides a 3D representation of the environment [18]. Although the specifics of implementation are not directly mapped one-to-one, since the goal of altimetry is not to estimate the radial velocity of the platform relative to the ground surface and a single range value is eventually reported as altitude, the overall flow of operations is largely applicable. The approach followed in this study is to leverage as much reference material from contemporary works as possible to focus efforts on uncharted areas rather than reinventing the wheel. Figure 2 contains a top-level diagram exhibiting the signal processing flow involved in point cloud generation. It is important to note that this is a generic model and is not specifically tailored for altitude estimation.

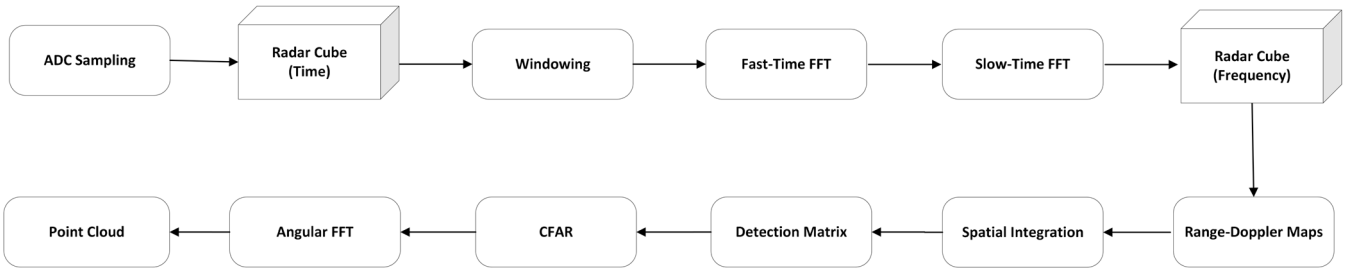

Figure 2. Signal processing flow for point cloud generation in automotive FMCW radars [36].

The central consideration at this stage is orchestrating the optimal FMCW chirp frame. A legacy FMCW-based RA is designed for range estimation only. Accordingly, one chirp per frame for a single pair of Tx and Rx antennae fulfills the requirement. On the contrary, AoA requires at least two receive antennae. Similarly, Doppler estimation is beyond the scope of Ras, and the rationale of using multiple chirps per antenna in a frame is to increase the SNR in the detection stage. Given the limited Tx power in automotive radars, necessary remediations are made in the waveform to compensate for very high free space propagation loss at 77 GHz frequency [37]. Aggregating multiple chirps per frame offers noncoherent integration gain when subject to the 2D-FFT.

3.3. The Radar Cube

The theory of FMCW chirp generation, propagation, and reception has been addressed in the preliminary work. This article focuses solely on the signal processing flow following the generation of beat frequencies corresponding to targets within the radar FOV. The radar cube is a convenient and efficient method for storing ADC samples per frame in the on-chip memory. The specifics of memory management and processing optimization are beyond the scope of this work. Nevertheless, interested readers may refer to the DSP implementation guide for an in-depth understanding [38]. Moreover, the arrangement of data is suitable for performing signal processing operations such as windowing, FFT, and CFAR detection on DSP. Lastly, it makes the presentation of space–time information visually compelling. It organizes measurements into a three-dimensional array, incorporating fast-time, slow-time, and spatial data. Subsequently, target characteristics including range, velocity, and angular position are evaluated [39]. It is important to understand that the radar cubes for time and frequency representations are different. The time-domain radar cube only contains the ADC samples, whilst the frequency counterpart comprises range-Doppler maps for each receive antenna.

The arrangement of the time-domain radar cube is shown in Figure 3. For the 3D matrix, each row of a single column represents an IF signal as a set of complex-valued ADC samples, referred to as the fast-time. The term fast-time corresponds to the high-frequency sampling rate required to capture the fine details of the time-of-flight, which is directly related to the range measurement. On the other hand, each column corresponds to the respective Doppler chirps within a single frame. The sampling interval along the columns is termed PRI. Typically, PRIs are much longer than the fast-time sampling interval; hence, this dimension is termed as the slow-time. The SWaP characteristics of mmWave automotive radars are largely attributed to the integrated antenna architecture in a single modular form factor. Each 2D fast-time, slow-time sub-matrix of the 3D radar cube corresponds to a unique receive antenna element, termed the spatial dimension.

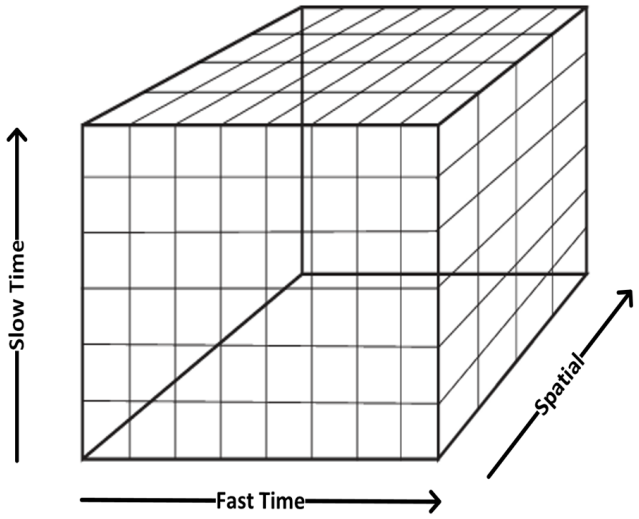

Figure 3. Radar cube exhibiting slow-time, fast-time, and spatial dimensions [39].

3.4. Windowing

Windowing prevents spectral leakage when the time-domain signal size is not an integer multiple of the FFT length, ensuring accurate frequency analysis [40]. It involves multiplying the input signal by a window function, reducing spectral leakage and improving frequency resolution. Rectangular and flat-top windows are unsuitable for altimetry due to closely spaced beat frequencies. Instead, Hamming, Hanning, and Blackman windows are preferred: Hamming balances main-lobe width and side-lobe levels, Hanning improves side-lobe suppression, and Blackman provides the best side-lobe roll-off. This study used the Blackman window for range processing in FFT, as its wider main lobe does not affect CFAR peak grouping. The time-domain function for the Blackman window is expressed as

$$w(n) = 0.42 - 0.5\cos\left(\frac{2\pi n}{N-1}\right) + 0.08\cos\left(\frac{4\pi n}{N-1}\right), \quad (1)$$

where N is the size of the input ADC sample space. The faster roll-off rate of this windowing function helps suppress noise in adjacent range bins lacking ground returns, making the choice of windowing method critical in the CFAR detection stage. However, with limited antennas and coarse angular resolution, windowing in the second FFT stage for Doppler processing offers minimal spatial benefit. While these windowing operations apply to both the cruise and landing approach stages, details for the touchdown stage are addressed separately in the respective section.

3.5. Range and Doppler FFT

FFT is an efficient spectral analysis tool used to compute the DFT of a time-domain signal. In radar applications, it plays a crucial role in range estimation by analyzing the frequency content of the IF signal. The structure of signals in FMCW radars, which use LFM

waveforms, is designed to facilitate spectral analysis and interpretation of beat frequencies. These frequencies indicate target distances based on the round-trip time of flight of signals reflected from objects within the radar field of view. The FFT is mathematically expressed as

$$X(k) = \sum_{n=0}^{N-1} x(n) \cdot e^{-j2\pi kn/N}, \quad (2)$$

where N is the FFT order and $X(k)$ is the frequency-domain representation of the time-domain signal, $x(n)$. Each sample of the FFT output corresponds to a specific range bin. The range-FFT in the context of a radar cube is extended for multiple Doppler chirps as [41]

$$X(k,\tau) = \sum_{n=0}^{N_R-1} x(n,\tau) \cdot e^{-j2\pi kn/N_R}, \tau = 0 \; to \; N_D - 1, \quad (3)$$

where $X(k,\tau)$ is the frequency-domain representation of the IF signal corresponding to k range bins for the Doppler chirp with index τ, while N_R and N_D are the order of range FFT and number of Doppler chirps, respectively. Doppler-FFT or slow-time FFT is used for estimating Doppler shifts caused by the motion of targets relative to the radar platform. While slow-time is essential in most automotive applications, it is largely irrelevant in radar altimetry, where the goal is altitude estimation rather than velocity measurement. However, Section 6 contains an important phenomenon of Doppler compensation in the case of TDM-MIMO, where Doppler estimation is important for resolving phase ambiguity arising from simultaneous motion and angular position at an offset from radar boresight. The mathematical expression for slow-time FFT is given by

$$Y(k,\tau) = \sum_{n=0}^{N_D-1} X(k,\tau) \cdot e^{-j2\pi kn/N_D}, k = 0 \; to \; N_R - 1, \quad (4)$$

where $Y(k,\tau)$ is the range-Doppler map for a single receive antenna. The aim is to noncoherently integrate multiple chirps per antenna per frame for an increased SNR that ensures an acceptable PFA. SNR enhancement is crucial in radar applications, particularly in mmWave automotive radars with limited Tx power. These aspects were detailed extensively in the preliminary work [5].

3.6. Chirp Integration and Detection Matrix

In the signal processing flow of an mmWave FMCW radar, the generation of the detection matrix marks a crucial stage just prior to the CFAR detection. This process involves collapsing the 3D radar cube containing separate range-Doppler maps for each receive antenna into an integrated range-Doppler map. The choice of coherent vs. noncoherent integration depends strictly on the scenario under consideration. Coherent integration combines multiple chirps coherently to enhance the signal power [42]. However, it requires stable phase relationships between consecutive chirps, which is challenging to maintain onboard a moving drone. On the other hand, noncoherent integration sums up the absolute value of individual chirps without regard to phase, making it more suitable for moving platforms while the enhancement in SNR is not as substantial.

3.7. Fundamentals of AoA Estimation

AoA refers to the direction from which a signal arrives at the receiver with respect to the radar boresight. AoA estimation typically requires at least two antennae. An SIMO radar system uses a single Tx antenna and multiple Rx antennae for AoA estimation. For instance, a system equipped with four Rx antennae achieves an angular resolution of approximately 28.64°, whereas one with eight Rx antennae achieves around 14.32°. Consequently, enhancing angle resolution requires increasing the number of Rx antennae. Figure 4 depicts a radar system with a single Tx antenna and two Rx antennae separated by a distance, d.

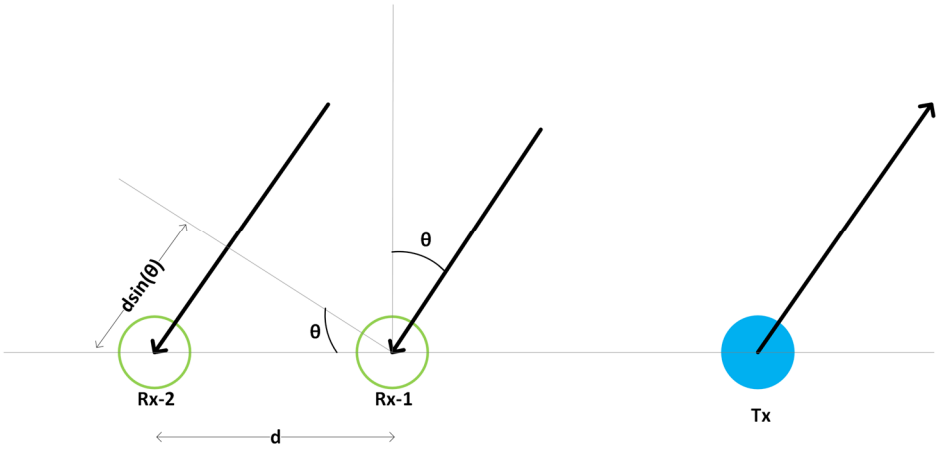

Figure 4. Fundamentals of AoA estimation in an SIMO radar [43].

The signal emitted by the Tx antenna is reflected off an object at an angle θ relative to the radar boresight and is subsequently received by both Rx antennae. The signal from the object covers an extra distance of $d\sin\theta$ to reach the Rx-2 antenna. The phase difference, denoted as ω, between the signals received at the two Rx antennae is

$$\omega = \frac{2\pi}{\lambda} d\sin\theta, \tag{5}$$

where λ and θ are the wavelength and angle of incidence, respectively. The expression $\frac{2\pi}{\lambda}$ is termed the wavenumber. Thus, by estimating the phase difference ω, it is possible to estimate the AoA as

$$\theta = \sin^{-1}\left(\frac{\omega\lambda}{2\pi d}\right). \tag{6}$$

Since the maximum unambiguous phase difference must be less than or equal to $|\pi|$, it follows from (6) that the maximum FOV, θ_{FOV}, can be achieved for an intra-antenna spacing of $\frac{\lambda}{2}$ as

$$\theta_{FOV} = \pm\frac{\pi}{2}. \tag{7}$$

In general, for a radar with N_{Rx} antennae, each subsequent antenna has an additional phase-shift of ω from the previous, forming a progressive series $[0\ \omega\ 2\omega\ \ldots N\omega]$. This periodic pattern can be estimated using a third stage of FFT, commonly referred to as the angular FFT. The frequency components in this FFT indicate the angular position of the target from the boresight of the radar. An object at radar boresight will cause all the antennae to receive the reflected returns at the same time, hence producing a DC component only. The mathematical expression for angular resolution in radians is given by

$$\theta_{RES} = \frac{2}{N_{Rx}}, \tag{8}$$

where N_{Rx} is the number of receiving antennae as well as the order of the angular FFT. The derivation of (8) is beyond the scope of this work, and interested readers may refer to [26] for an in-depth understanding. Equation (8) signifies that very fine angular resolution can be achieved by increasing N_{Rx}. However, there are limitations to achieving that from a volumetric, cost, and complexity standpoint. Section 6 contains a dedicated discussion on the concept of TDM-MIMO to overcome this challenge while increasing the angular resolution at the same time. At this stage, the aim of the preceding discussion was to elaborate on the concept of AoA and underscore the inherent limitation in increasing the N_{Rx} beyond a certain limit.

4. Overview of Methodology

This work continues from the preliminary article, focusing on optimizing performance metrics within the hardware limitations of mmWave automotive radars. The preceding work argued that operational requirements and interrelated performance metrics eventually dictate the parameters of FMCW waveforms. This article examines these dynamic requirements across the three flight stages, with the operational needs of each stage summarized in tables followed by derived waveform specifications listed separately. Since each stage has unique requirements, the associated signal-processing aspects are also unique to the respective stage. For instance, the concept of TDM-MIMO is unique to the landing approach stage, while the ZFFT algorithm is discussed only for the touchdown stage. Each stage is simulated as a scenario in MATLAB using the Radar Toolbox. The simulation results are presented along with mathematical and theoretical elucidations to consolidate the arguments.

5. Cruise

The cruise stage for an airborne platform is defined as the level flight segment after arrival at the initial cruise altitude until the start of the descent to the destination [44]. In the context of UASs, this is the stage of flight where a designated task is performed. For applications requiring the UAS to maintain a constant altitude AGL, RAs are mandatory. As already explained in the preceding text, the main purpose of an RA is the real-time estimation of altitude AGL. The authors' preliminary study orchestrated a realistic test case to maximize the range with the finest possible resolution. It is pertinent to note that although velocity estimation is not an inherent objective, the variations in aircraft altitude and terrain profile introduce a radial velocity component [45]. It is crucial to characterize and remediate the impact of this component on altitude estimation. To this end, terrain models were adopted from MATLAB [46]. Figure 5 shows the standard deviation in terrain elevation for various land types.

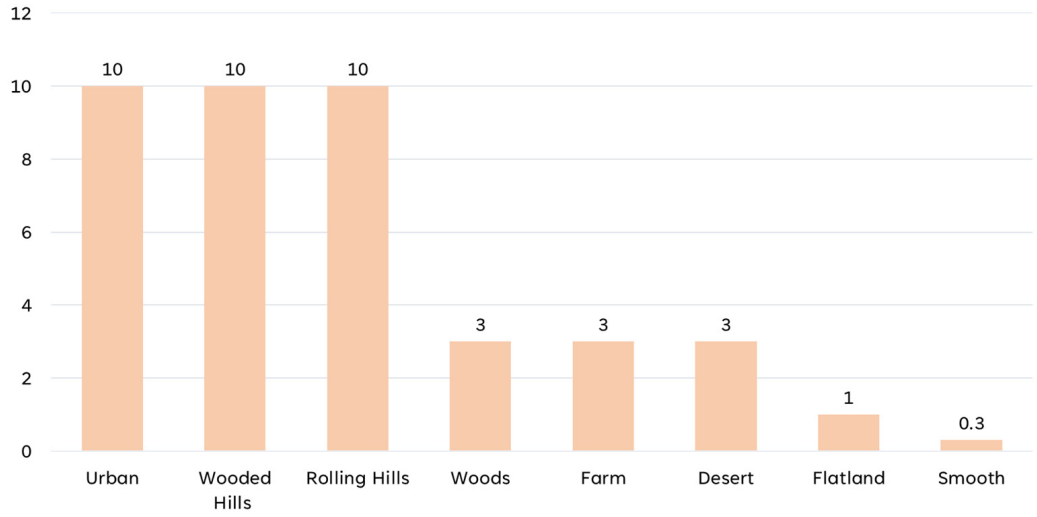

Figure 5. Standard deviation in terrain elevation for various land types [46].

Due to the unavailability of step size, it was considered appropriate to consider it equal to the lateral motion covered by the drone in one second. Accordingly, for a lateral velocity of 20 m/s, the terrain exhibits an altitude variation of 10 m. Consequently, the radial velocity component equates to 10 m/s. This represents a stringent requirement aimed at catering to a worst-case scenario. The operational requirements for the cruise phase are listed in Table 2, with Table 3 containing the resultant waveform specifications.

Table 2. Operational requirements for the cruise stage.

Requirement	Value	Remarks
R_{acc}	$\pm$0.45 m	Range Accuracy
R_{min}	150 m	Minimum Altitude
R_{max}	300 m	Maximum Altitude
V_{lat}	20 m/s	Maximum Lateral Velocity
σ_h	10 m	Maximum Standard Deviation of Terrain
V_{rad}	10 m/s	Maximum Radial Velocity
SNR_{min}	20 dB	Minimum SNR Requirement
T	0 °C	Antenna Temperature

Table 3. Resultant waveform parameters for the cruise stage.

Parameter	Value	Remarks
Δt_{max}	3.6653 s	Max Time B/W Data Updates
U_{min}	0.2728 Hz	Minimum Update Rate
T_c	1 ms	Chirp Duration
B	1 GHz	Chirp BW
$\Delta R(B)$	0.15 m	Function of Chirp BW
IF_{max}	3 MHz	Maximum Beat Frequency for Max Range
F_s	3.33 MSPS	Sampling Rate in Mega Samples Per Second
S	1 MHz/µs	Chirp Slope
N_{FFT}	4096	FFT Size
Δf	805.66 Hz	Frequency Resolution
$\Delta R(F_s, N_{FFT}, S)$	0.13 m	Function of Sampling Rate, FFT, and Slope
N	16	Number of Chirps/Frame
T_F	16 ms	Frame Duration
$V_{\max}$	0.974 m/s	Maximum Unambiguous Velocity
N_{Tx}	1	Number of Transmit Antennae
N_{Rx}	4	Number of Receive Antennae
θ_{res}	28.64°	Angular Resolution
B_n	62.5 Hz	Noise Bandwidth
P_n	$-$141.27 dBm	Noise Power
σ_0	2.47	NRCS
$R_{max}(SNR_{min})$	4586 m	Function of Minimum SNR
$R_{max}(IF_{max}, S)$	450 m	Function of IF, BW, and Slope
$R_{max}(N_{FFT}, \Delta R)$	540 m	Function of FFT and Resolution
Alt_{max}	450 m	Maximum Measurable Altitude

These limitations laid the foundation for waveform design in the preliminary study as well. It was argued in the proceeding discussion that these limitations affect the performance of RAs from a signal-processing standpoint as well. It was exhibited in previous work that the choice of a longer chirp duration aids in reducing noise BW while simultaneously allowing for an IF filter with relatively narrower BW to cater to a high-altitude requirement. It is made possible by using a gradual chirp slope to achieve the same chirp BW with a longer chirp duration. This allows for a higher value of maximum range without compromising the range resolution. However, this upper bounds the $V_{\max}$ to a very small value, leading to Doppler folding with target velocity aliasing into neighboring Doppler bins. The scenarios were simulated using the Radar Toolbox in MATLAB (see Figure 6) and it was observed that for a radial velocity component of 10 m/s, the range profile predominantly appeared in the 0th Doppler bin. This approach of empirical validation aligns well with the scope of the application, since 10 m/s represents a worst-case scenario, since actual radial velocities are expected to be significantly lower. Consequently, the 0th Doppler bin was selected as the range profile for the subsequent stage of CFAR detection, ensuring consistent detection performance.

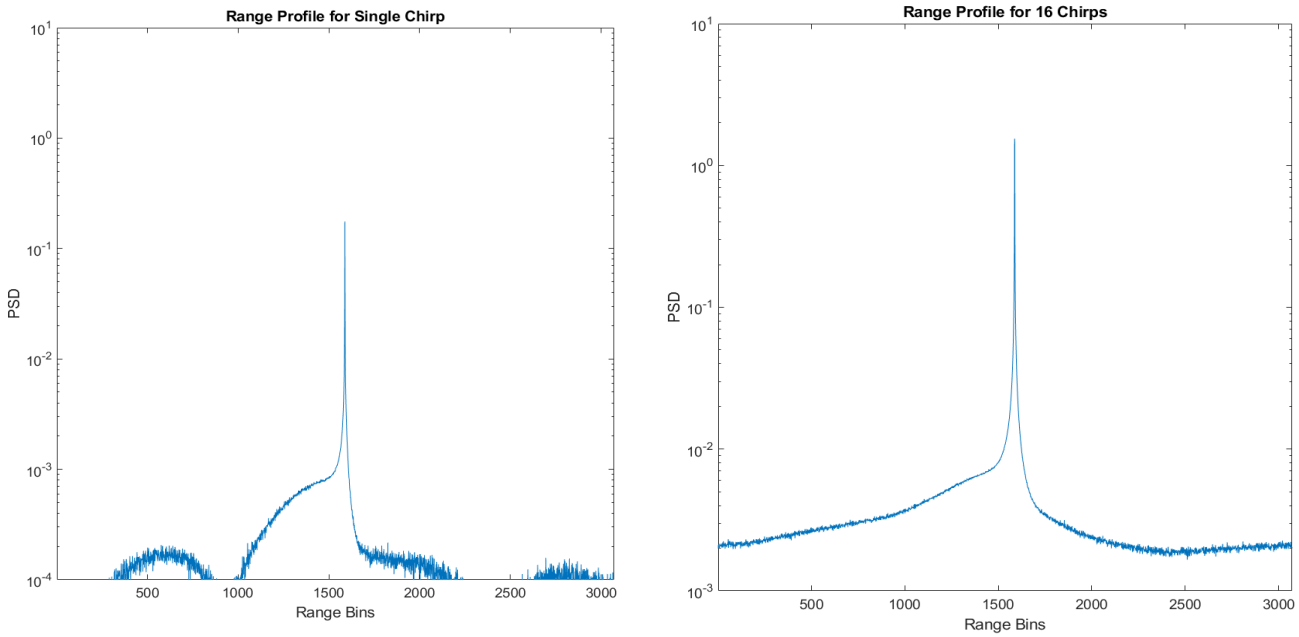

(**a**) (**b**)

Figure 6. Comparison of range profile: (**a**) Single chirp per frame; (**b**) 16 chirps per frame.

Nevertheless, a long chirp duration has its own inherent limitations. While the range profile resides in the 0th Doppler bin, the radial velocity component causes the target to be distributed across multiple range bins. This phenomenon is illustrated in Figure 7 for a single target, where the peak is spread over multiple neighboring bins. For a velocity of 10 m/s, the target moves 1 cm over a chirp duration of 1 ms. Point cloud data are exported from the radar at the end of each FMCW chirp frame, governing the update rate. Consequently, over the span of 16 chirps with a total duration of 16 ms, the cumulative distance covered is 16 cm. Given a range resolution of 10 cm, the target will spend a duration of 10 ms in the initial range bin and 6 ms in the neighboring bin either to the right or left, depending on the direction of relative radial motion. The only drawback of a very long chirp duration in the cruise stage is, therefore, measurement accuracy being compromised by a maximum value of 10 cm. Considering a range accuracy requirement of 45 cm, as specified in Table 2, this trade-off is acceptable within the scope of the hardware limitations since the range resolution only degrades by a maximum cumulative value of 20 cm.

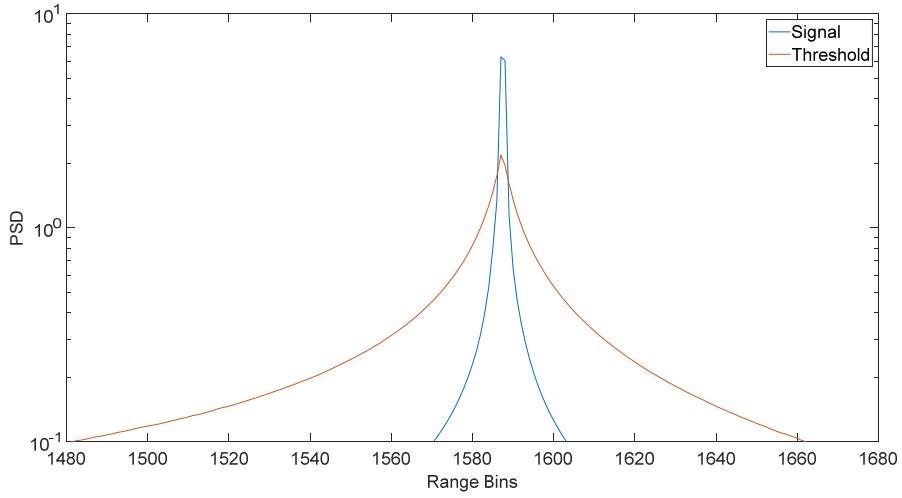

Figure 7. Range profile and CFAR threshold.

5.1. CFAR for Detection of Ground Surface

Once the range profile is acquired, the next step is to determine whether the peaks in the FFT range profile correspond to the ground surface. The detection technique employed for this study is the CFAR algorithm. It maintains a constant false alarm rate by dynamically adjusting the detection threshold based on the noise level. This approach helps in the identification of ground surface in the presence of clutter due to specular reflection. This is particularly important for the intended application since the target is the surface of the ground with a varying terrain elevation profile.

There are three major variants of the CFAR algorithm based on how the noise threshold is calculated: CFAR-CA, CFAR-CASO, and CFAR-CAGO. CFAR-CA uses the average noise level from both sides of the target cell to evaluate the detection threshold, while CFAR-CASO and CFAR-CAGO modify this approach by using the smallest and greatest average noise levels from the training cells, respectively, from either side of the target cell. Guard cells, on the other hand, are the ones adjacent to the target cell that help prevent signal leakage from the target cell into the noise estimation process. The guard cells are deliberately excluded from the noise estimation to ensure that the presence of the target signal does not bias the noise estimation, leading to a more accurate approximation. The mathematical expression for the noise level in CFAR-CA is given by

$$N_{CA} = \frac{1}{2N_T}\sum_{k=1}^{2N_T} N(k), \tag{9}$$

where N_T is the number of training cells on either side of the kth target cell, $N(k)$. While straightforward from an implementation standpoint, it can be less effective in environments with significant variation in terrain profile. Appropriately, CFAR-CASO is better suited for rough terrains. The mathematical expressions for noise level on the left and right side of the target cell in CFAR-CASO are given by [3]

$$N_L = \frac{1}{N_L}\sum_{k=1}^{N_L} N(k), \tag{10}$$

$$N_R = \frac{1}{N_R}\sum_{k=1}^{N_R} N(k), \tag{11}$$

The smallest of the two averages is eventually chosen to be the noise level as follows:

$$N_{CASO} = \min(N_L\,, N_R) \tag{12}$$

The CFAR algorithm, by keeping a constant threshold, calculates the detection threshold as a function of the PFA [47]. The scaling factor for estimating the threshold factor is expressed as

$$\alpha = N_{CASO}\left(PFA^{-\frac{1}{N_{CASO}}} - 1\right), \tag{13}$$

It is evident from (13) that a small value of PFA signifies a higher value of the scaling factor. Subsequently, the threshold for the kth cell is given by

$$T(k) = \alpha \times N_{CASO}(k), \tag{14}$$

For all the target cells with signal amplitudes above the threshold, a target matrix containing binary elements is generated as

$$V(k) = \begin{cases} 1, & V(k) > T(k) \\ 0, & otherwise \end{cases}, \quad k = 0,\ 1,\ 2,\ 3 \ldots N_{FFT} \tag{15}$$

where $V(k)$ is the kth target cell of the range profile with a size equal to the order of the range FFT, N_{FFT}. Like any detection method, CFAR-CASO is employed to validate potential target returns and to ensure that statistically significant targets are considered,

effectively reducing false alarms. Figure 8 shows a side-by-side comparison of the CFAR variants under discussion for a ground surface, offering five unique targets indicative of rough terrain. It is apparent that CFAR-CASO has a higher detection threshold but is still able to detect more targets. This indicates a lower PFA while still being able to detect more targets with a better approximation of noise. In conclusion, while CFAR-CA provides a straightforward approach to target detection, the ability of CFAR-CASO to handle clutter more effectively makes it the preferred choice for RAs operating over terrains with varying elevation profiles. Discussion on CFAR-CAGO has been deliberately skimmed due to its limited applicability to the intended use case.

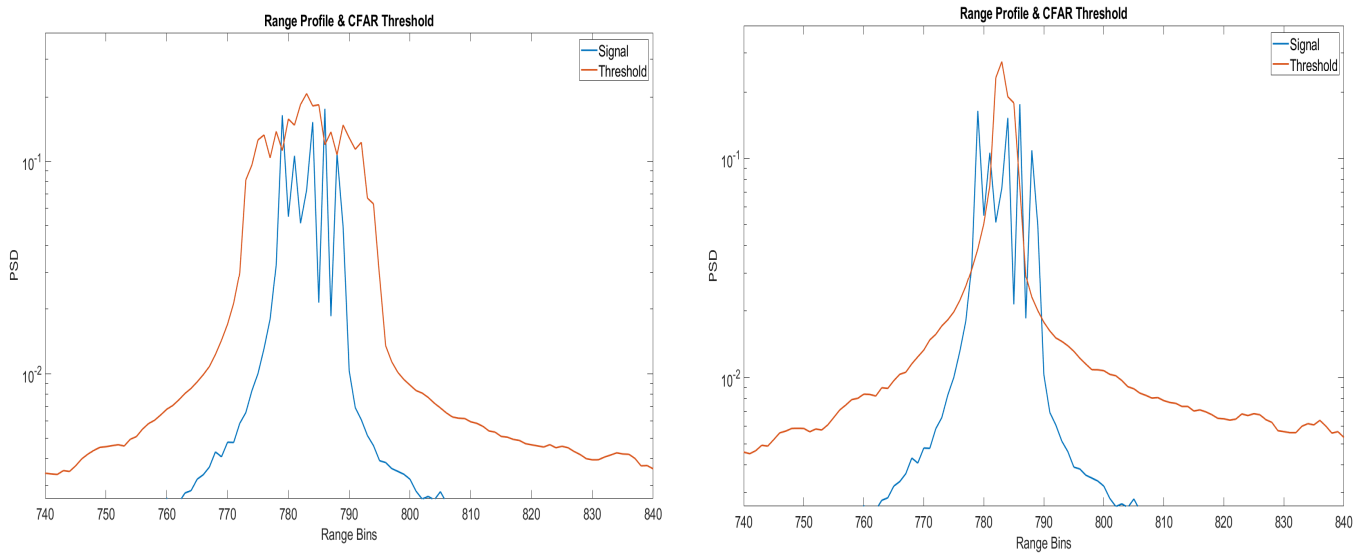

Figure 8. Range profile and CFAR threshold: (**a**) CFAR−CA; (**b**) CFAR−CASO.

The altimetry application requires that only a single valid target is reported as the altitude of the drone. Fittingly, it is essential to identify the strongest target return from a set of validated targets as the ground surface. Given that the radiation pattern of the IWR1843BOOST features a single grating lobe, the strongest return is expected from the ground surface at the radar boresight [16]. The peak grouping methodology coupled with the antenna characteristics favors accurate altitude reporting.

5.2. Utility of SIMO for High Altitude

Albeit having high altitude requirements, having multiple receive antennae may be leveraged for AoA estimation. It can be particularly useful in filtering ground returns from off-boresight angles and better approximation of true altitude. Another inherent benefit of multiple Rx antennae is that even if the AoA capability is not utilized, integration of FMCW chirps along the antenna dimension improves SNR. Increased SNR is a desirable scenario for high-altitude estimation.

Since there is considerable signal processing overhead, it is appropriate to appraise the benefit of incorporating SIMO in the cruise stage. Figure 9 illustrates the radar platform, IWR1843, onboard a drone cruising at an altitude of 180 m. A simplified scenario is elucidated, with a hilltop and flat terrain being point A and B, respectively. Given the minimum altitude requirement of 150 m, an arbitrary value of p is chosen to be 180 m. Appropriately, the Pythagorean theorem can be applied for the evaluation of the base length, Δd. For both points to be identified as separate targets in the angular domain, θ is considered equal to angular resolution, θ_{res}, 28.64°. Consequently, the requirement of minimum separation, Δd, between points A and B amounts to approximately 98.3 m. This shows that the 1×4 SIMO configuration offers little to no value in terms of angular information. The only benefit of having multiple antennae is, therefore, the SNR improvement through noncoherent

integration along the antenna dimension. The 2D range-Doppler map in (4) was provided for a single antenna. The same expression can be extended for multiple antennae. The SNR-enhanced version commonly referred to as the detection matrix is mathematically expressed as

$$D(k,\tau) = \sum_{a=1}^{N_{Rx}} |Y(k,\tau,a)|, \tag{16}$$

where $Y(k,\tau,a)$ corresponds to range-Doppler maps for antenna index a, and $|.|$ is the absolute value of the complex entries in the respective maps. The detection matrix is better suited for CFAR detection owing to the improved SNR, mathematically expressed as

$$P_{\text{int}} \approx N_{\text{Rx}} \cdot P_{\text{a}}, \tag{17}$$

where P_{int} and P_{a} signify the signal power before and after integration. As the phase is not summed coherently, the gain is scaled only by a factor of N_{Rx}.

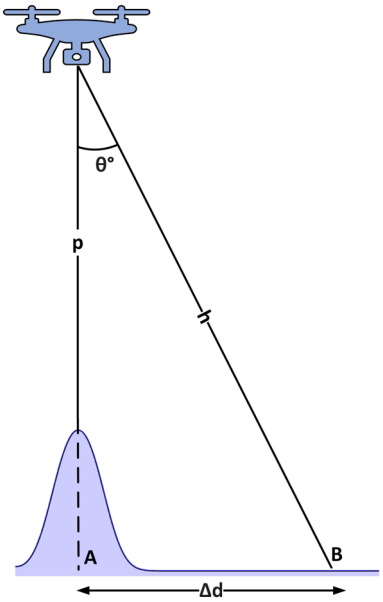

Figure 9. AoA estimation at high altitude.

6. Landing Approach

The intrinsic utility of RAs in the aviation industry is in the landing approach stage to aid navigation by providing altitude AGL. This section endeavors to establish the efficacy of AoA estimation using TDM-MIMO for achieving high angular resolution while leveraging the SWaP characteristics of mmWave automotive radars. The aim is to utilize high angular resolution for improved situational awareness during the autonomous landing of UASs in tough scenarios. The concept of TDM-MIMO and virtual antennae is covered in much detail from a theoretical and mathematical perspective. Subsequently, the specifics of Doppler estimation and compensation in TDM-MIMO radars are discussed. Eventually, two corner cases of a drone landing on a ship are emulated as an application of TDM-MIMO for enhanced situational awareness.

6.1. TDM-MIMO for High Angular Resolution

The discussion on SIMO radars highlighted that the angular resolution improves with an increase in the number of receive antennae. However, there is a limit to increasing the number of receive antennae. To double the angle resolution, the number of Rx antennae must also be doubled. However, the addition of antennae not only entails volumetric overhead but also necessitates separate receiver chains within the device, including, but not limited to, LNA, mixers, IF filters, and ADC. The foundation of preliminary work was based on the excellent SWaP characteristics of the automotive radars and the significantly

low cost of production. Appropriately, MIMO radars are an effective method for doubling the θ_{RES} with the addition of only one Tx antenna.

Figure 10 depicts a radar system with two transmit antennae. It must be remembered that intra-antenna spacing, d, is $\lambda/2$, as elaborated in the concept of the SIMO radar. The transmission from Tx1 produces a phase of $[0\ \omega\ 2\omega\ 3\omega]$ at the four Rx antennae. Due to the placement of Tx2 at a distance of $4d$ from Tx1, any signal transmitted from Tx2 travels an extra distance of $4d\sin\theta$ compared to Tx1. Similarly, the signal received at each receive antenna experiences an additional phase shift of 4ω compared to the transmission from Tx1. The signal phase at the four receive antennae, caused by a transmission from the Tx2, is, therefore, $[4\omega\ 5\omega\ 6\omega\ 7\omega]$. The phase sequences at the four Rx antennae resulting from the transmissions by Tx1 and Tx2 yield a concatenated sequence $[0\ \omega\ 2\omega\ 3\omega\ 4\omega\ 5\omega\ 6\omega\ 7\omega]$, which is identical to the sequence observed for one Tx and eight Rx antennae, as shown in Figure 11. The 2Tx–4Rx antenna configuration essentially creates a virtual array of eight Rx antennae. In summary, by utilizing $N_{\mathrm{T}x}$ and $N_{\mathrm{R}x}$ antennae and ensuring appropriate placement, a virtual antenna array of size $N_{\mathrm{T}x}$x$N_{\mathrm{R}x}$ is formed.

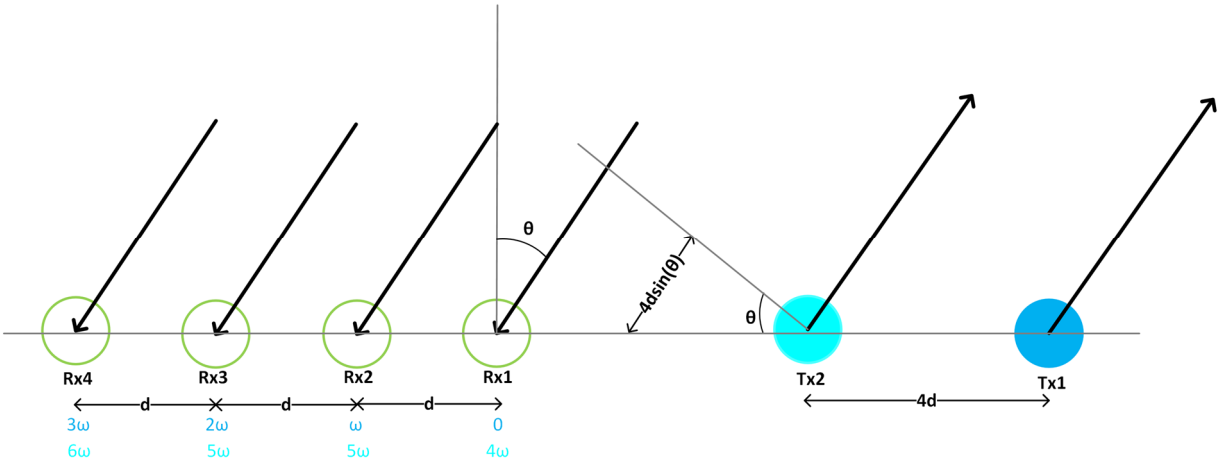

Figure 10. 2Tx–4Rx virtual antenna array in an MIMO radar.

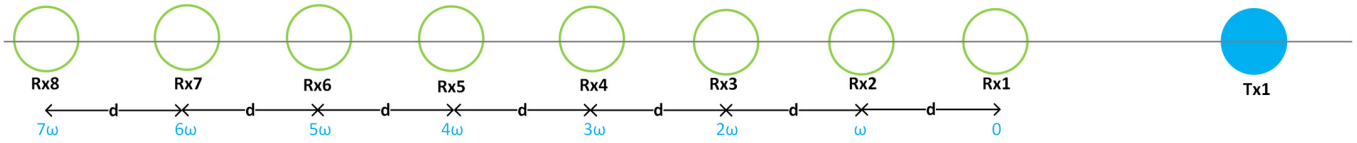

Figure 11. 1Tx–8Rx physical antenna array in an SIMO radar.

This significant increase in the number of virtual antennae leads to an enhancement in the angular resolution. Figure 12 exhibits radiation patterns of SIMO and MIMO antenna configurations. It is evident that the combined beam-width for both configurations is the same; however, MIMO achieves this with a total of six antennae in contrast to nine elements in SIMO. This allows for a significant saving both in terms of volume as well as complexity of the radar chip. It is crucial to emphasize that the radars must be able to distinguish and isolate the signals coming from different Tx antennae. Two approaches that are prevalent in the literature are TDM and BPM [26]. For the sake of this study, TDM-MIMO was preferred over BPM-MIMO due to the simplicity of implementation. Both techniques are largely unexplored in the context of mmWave altimetry for UASs, making TDM-MIMO an appropriate choice for initial exploration. BPM-MIMO offers a 3 dB SNR improvement for the antenna configuration in IWR1843. However, this improvement holds little value since MIMO is employed only in the landing approach in close proximity to the ground surface. Consequently, the added benefit of BPM-MIMO is minuscule, justifying the decision to proceed with TDM-MIMO for its straightforward implementation and equally adequate

performance in terms of angular resolution. The requirements for the landing approach stage are listed in Table 4.

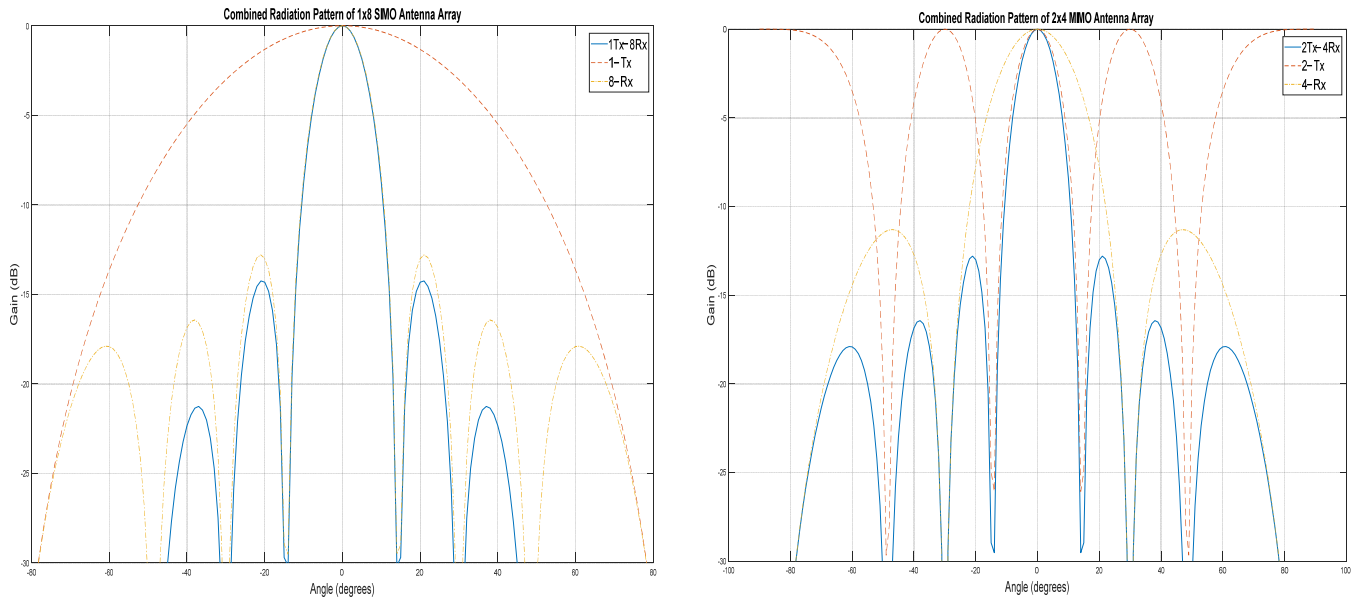

(**a**) (**b**)

Figure 12. Combined radiation patterns: (**a**) 1 × 8 SIMO; (**b**) 2 × 4 MIMO.

Table 4. Operational requirements for the landing approach stage.

Requirement	Value	Remarks
R_{acc}	±0.45 m	Range Accuracy
R_{min}	5 m	Minimum Altitude
R_{max}	150 m	Maximum Altitude
V_{lat}	20 m/s	Maximum Lateral Velocity
RoD	5 m/s	Maximum Rate of Descent
σ_h	2 m	Maximum Standard Deviation of Terrain
V_{rad}	7 m/s	Maximum Radial Velocity
SNR_{min}	20 dB	Minimum SNR Requirement
T	5 °C	Antenna Temperature

For TDM-MIMO, the orthogonality is in the time domain. Each frame is composed of multiple blocks, and each block is composed of N_{Tx} time slots. Each time slot corresponds to the transmission by one of the N_{Tx} antennae. Figure 13 illustrates the allocation of time slots for Tx1 and Tx2 in an FMCW chirp frame for $N_{Tx} = 2$. The range-Doppler maps for each virtual antenna are integrated noncoherently using (16) to create a detection matrix. Afterward, CFAR-CASO detection from (15) is employed to identify valid targets. It is important to note that the angular FFT may only be applied to the objects designated as legitimate targets by the CFAR algorithm, rather than all the bins of the detection matrix. This approach allows for a significant optimization in implementation.

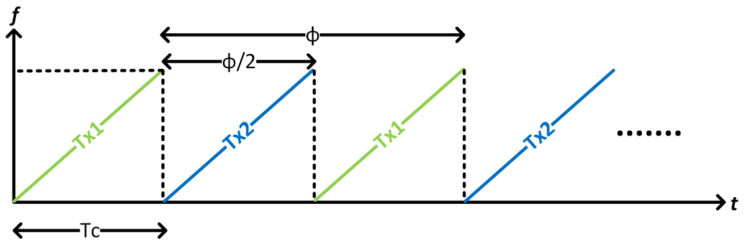

Figure 13. TDM-MIMO chirp frame with Doppler induced due to radial velocity.

The reason for using the detection matrix lies in the enhanced SNR due to integration along the antenna dimension leading to improved CFAR detection performance. Prior to that, it is necessary to perform a Doppler correction step to adjust for any phase change caused by the radial velocity component due to the ROD relative to the ground surface. The 0th Doppler bin, $D(k,1)$, for $\tau = 1$ from (16) being the range profile is subject to CFAR-CASO detection. The next step is to identify the peaks along the slow-time dimension corresponding to the range bins, k_i, identified as valid targets. The mathematical expression estimating the Doppler bin index, τ_i, is given by

$$\tau_i = arg\underset{\tau}{max}\, D(k_i, \tau),\ \tau = 1, 2, 3 \ldots N_{Dopp}, \tag{18}$$

where *argmax* function returns the index of the Doppler bin containing the peak. The phase difference, φ, is expressed as

$$\varphi = \frac{2\pi\tau_i}{N_{Dopp}}, -\frac{N_{Dopp}}{2} < \tau_i < \frac{N_{Dopp}}{2} - 1. \tag{19}$$

Figure 14 shows the phase difference due to radial velocity relative to the ground surface, φ, between two consecutive chirps corresponding to the same antenna, Tx1. The justification behind Doppler-induced phase compensation is that all the receiving antennae corresponding to Tx1 receive respective returns from the target at the same time. The only phase difference is due to the time of arrival at the respective antenna owing to the angular position of the target with respect to the radar boresight. However, there is an ambiguity in the phase difference between the two sets of receiving antennae corresponding to Tx1 and Tx2. It cannot be ascertained that the phase difference occurred either due to relative motion, the angular component, or both. The symmetric nature of the FMCW chirps arranged in the time domain one after the other without intra-chirp duration considerably simplifies the problem statement. Given that φ between chirp 1 and chirp 3 corresponding to Tx1 is due to the relative motion, the phase difference between chirp 1 and chirp 2 is given by

$$\delta = \frac{\varphi}{2}, \tag{20}$$

where δ is the phase difference due to relative motion and must be compensated. It is pertinent to note that the correction is only to be applied to the virtual receive antennae corresponding to Tx2. Moreover, the correction is only applied to the bins corresponding to valid targets in the range-FFT. The virtual antennae ranging from index 1 to 4 do not warrant any correction. For virtual antennae ranging from 5 to 8, the corrected range FFT is expressed as

$$\overline{X(k_l, \tau_l, v)} = X(k_i, \tau_i, v).e^{-j\delta}, \quad v = 5, \ldots, 8, \tag{21}$$

where $e^{-j\delta}$ is the phasor corresponding to the phase compensation. Equation (21) signifies an interesting phenomenon, that the use of TDM-MIMO requires considerably accurate Doppler estimation followed by compensation to resolve the phase ambiguity due to simultaneous relative motion and angular position. Aptly, $V_{\max}$ must be chosen to incorporate the maximum ROD of the drone during the landing approach stage. For this endeavor, the value of ROD was chosen to be 5 m/s, as most commercial VTOL UASs operate within that range [48]. Since the proposed mmWave RA waveform aims to benefit a wide range of UASs, fixed-wing counterparts must also be considered. In the absence of specific data, an ROD value of 1000 feet per minute (approximately 5 m/s) for a lightweight propeller aircraft was selected, given similar flight dynamics [49]. However, $V_{\max}$ is an important factor since TDM-MIMO is employed for AoA estimation. In the event of a radial velocity component exceeding $V_{\max}$, Doppler-induced folding is bound to introduce unresolvable ambiguity and must be avoided. For a reduced requirement of the maximum range in the landing approach stage, there is room for reduction in the chirp duration to incorporate the maximum ROD. Section 9 contains a discussion on potential solutions to this limita-

tion to be explored in the next stage of research. Table 5 contains the resultant waveform parameters derived in accordance with the requirements of the landing approach stage.

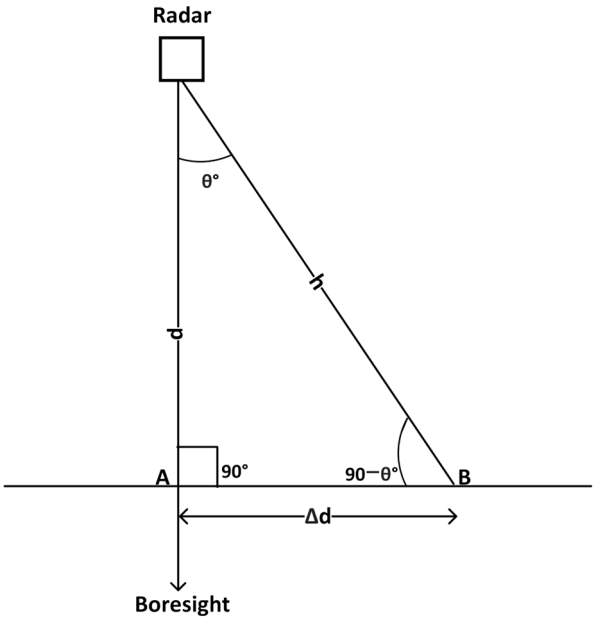

Figure 14. VTOL UAS landing on a drone ship surrounded by water.

Table 5. Resultant waveform parameters for the landing approach stage.

Parameter	Value	Remarks
Δt_{max}	0.1223 s	Max Time B/W Data Updates
U_{min}	8.14 Hz	Minimum Update Rate
T_c	140 µs	Chirp Duration
B	1 GHz	Chirp BW
$\Delta R(B)$	0.15 m	Function of Chirp BW
IF_{max}	10 MHz	Maximum Beat Frequency for Max Range
F_s	12.5 MSPS	Sampling Rate in Mega Samples Per Second
S	7.1 MHz/µs	Chirp Slope
N_{FFT}	2048	FFT Size
Δf	6103 Hz	Frequency Resolution
$\Delta R(F_s, N_{FFT}, S)$	0.11 m	Function of Sampling Rate, FFT, and Slope
N_{Dopp}	32	Number of Chirps/Frame
T_F	4.48 ms	Frame Duration
N_{Tx}	2	Number of Transmit Antennae
N_{Rx}	4	Number of Receive Antennae
θ_{res}	14.32°	Angular Resolution
B_n	223.21 Hz	Noise Bandwidth
P_n	−135.74 dBm	Noise Power
σ_0	2.47	NRCS
$R_{max}(SNR_{min})$	2426 m	Function of Minimum SNR
$R_{max}(IF_{max}, S)$	211 m	Function of IF, BW, and Slope
$R_{max}(N_{FFT}, \Delta R)$	264 m	Function of FFT and Resolution
Alt_{max}	211 m	Maximum Measurable Altitude

6.2. TDM-MIMO for Enhanced Situational Awareness

Expanding upon the fundamental principles of TDM-MIMO described earlier, this section covers its application in improving situational awareness of UASs during autonomous landing. It was demonstrated in Section 5.2 that the SIMO configuration for high altitude offers little to no value in terms of angular information. The scenario under consideration involves the landing of a small-sized VTOL drone on a ship surrounded by water on all sides.

Figure 14 shows the landing scenario where points A and B are sea and concrete ship surfaces, respectively. Both surface types are separated by a distance, Δd. Two corner cases are considered having dimensions listed in Table 6, with the first scenario having an AoA, θ, of 14.32° when both targets are in neighboring range bins, with points A and B at ranges of 4.67 m and 4.82 m from the radar, respectively. This is the closest difference in range that can be achieved for the given range resolution, and AoA, θ, is equal to the angular resolution, θ_{res}. The rationale behind orchestrating this scenario is to attempt identification of both surface types as distinct targets and use AoA to identify the angular position of the concrete surface. In the second scenario, the concrete surface is at maximum off-boresight angular position, while the sea surface is directly at the radar boresight. Accordingly, the difference in range increases with the point B moving to a range of 8.63 m. Before delving into the specifics of the second scenario, it is important to understand the difference of RCS for the concrete surface and the clutter due to the reflectivity of the sea surface. Devising clutter models for an mmWave source is a challenging task and it is convenient to consider reference models from the literature on sea clutter estimation. The authors' preliminary study covered clutter estimation in reasonable mathematical and theoretical detail. A similar approach is adopted here for the sea surface. The *seareflectivity* function from MATLAB offers a variety of reference models from authentic books on sea clutter estimation. The TSC empirical model [50] closely approximates the requirements for an mmWave radar altimeter operating at 77 GHz with a grazing angle, $\psi°$, of 90°. For the concrete surface of the ship, the NRCS was calculated based on the workings in the preliminary study using the Johns Hopkins University APL model [51]. The reflectivity of the sea depends on the scale factor of its surface, which essentially signifies that the higher the wind speed and tide, the greater the roughness of the sea surface and the higher the reflectivity.

Table 6. Dimensions for Figure 14.

p	h	Δd	$\theta°$	Remarks
4.67	4.82	1.19	14.32	Objects in Neighboring Range Bins
4.67	8.63	7.26	57.28	Maximum Off-Boresight Angular Position

An accurate emulation of real-world scenarios is imperative, and the highest value of NRCS for sea surface is expected to create more difficulties in differentiating the concrete surface of the drone ship from the sea surface. It is also worth mentioning that wind conditions indicative of a sea storm would prevent a small-sized VTOL drone from flying, let alone landing safely; therefore, a moderate value of scale factor was chosen. The respective grazing angles for both scenarios are different, and the ship is positioned at an offset from radar boresight such that a reduced grazing angle lowers the NRCS. It should be recalled that the grazing angle is the 90° complement of the angle of incidence or the intended AoA. The mathematical equations for clutter models were intentionally skimmed to limit the discourse to the application context only. Interested readers are encouraged to refer to the cited references of respective models for thorough understanding. The azimuthal and elevation HPBW values were taken from the specifications of IWR1843BOOST [16]. The operational requirements and resultant RCS values for both scenarios are listed in Table 7.

Table 7. RCS comparison of targets for scenarios under consideration.

Parameter	Sea	Scenario 1	Scenario 2	Remarks
Range (m)	4.67	4.82	8.63	Range of Respective Targets
ψ	90°	75.68°	32.72°	Grazing Angle
θ_a		56°		Azimuthal HPBW
θ_e		28°		Elevation HPBW
State	5	N/A	N/A	Roughness Index of Sea Surface
Model	TSC	APL	APL	Model for Clutter Estimation
NRCS	0.008	20.35	0.9506	Reflectivity Index
RCS (m^2)	0.052	135.49	11.34	Radar Cross-Section

It indicates that despite a higher grazing angle and shorter range of the sea surface compared to the concrete counterpart, the RCS values are drastically lower in both scenarios. However, there is a much lower RCS value for concrete surface owing to a lower grazing angle, ψ°, with the target moving significantly farther from the radar due to high off-boresight angular position. For the first scenario, the CFAR-CASO algorithm along with peak grouping will result in the sea surface not being detected as a valid target. The problem statement becomes significantly simpler and the only task that remains is to estimate the AoA for the highest peak in the range profile. The second scenario allows the sea surface to be detected after CFAR-CASO, but the significantly higher return from the concrete surface can still be easily identified. In summary, the massive difference in RCS between concrete and sea surface allows convenient AoA estimation using TDM-MIMO. At this stage, angular FFT is applied, followed by peak detection to estimate the presence of the concrete surface of the ship in the angular bin. Figure 15a,b show the concrete surface in respective angular bins for the first and second scenario, respectively. The high angular resolution offered by TDM-MIMO allows for enhanced situational awareness for landing in tough scenarios, including high-relief land surfaces as well. For the sake of this study, TDM-MIMO was only implemented in the azimuthal plane owing to the more feasible arrangement of the Tx and Rx antennae on the IWR1843BOOST.

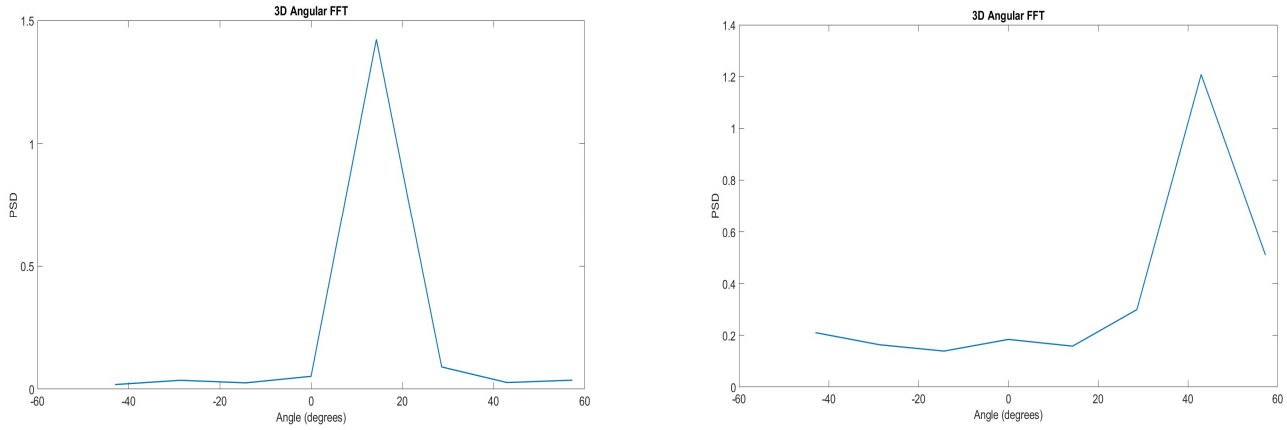

(**a**) (**b**)

Figure 15. Angular FFT showing peaks in respective bins: (**a**) Scenario 1; (**b**) Scenario 2.

7. Touchdown

WoW systems play a crucial role in the touchdown stage of aircraft, facilitating prompt control actions and safety measures. Precise assessment of the touchdown instant is crucial, necessitating failsafe mechanisms with multiple layers of redundancies. SWaP characteristics are crucial for the endurance of UASs. Appropriately, software redundancies provide a practical option, requiring little to no additional resources. By leveraging the software-defined architecture, radar waveform specifications can be customized to accurately detect touchdown instant aligning with the concept of software redundancy. Contrary to the conventional use of ZFFT focused on resource conservation, this section introduces an improvised utilization of ZFFT for achieving mm-level precision in range measurements.

7.1. Background

In the preliminary work, it was demonstrated that increasing the chirp bandwidth enhances the range resolution. However, while the physical principle of range resolution is influenced by chirp bandwidth, the spectral resolution governed by the FFT order must be sufficiently fine to fully utilize the benefits of wider bandwidth. However, there are computational limitations associated with increasing the FFT order while maintaining a high update rate, due to the extensive number of multiplication and addition operations involved. Efficient resource utilization is essential to balance high performance and com-

putational complexity. The use of ZFFT in providing mm-level accuracy for liquid-level sensing has been reported in the literature [21]. This section aims to appraise the possibility of tailoring waveform specifications in tandem with using ZFFT in the signal-processing stage to achieve mm-level accuracy. Ultrasonic sensors are prevalent in automotive parking assistance due to their affordability and effectiveness at a short range, facilitated by the relatively slower speed of sound compared to EM waves [52]. However, they are sensitive to environmental factors like temperature, humidity, and reverberation [53]. On the other hand, radars are oblivious to these factors. Although RAs have been utilized for touchdown detection in commercial aircraft [54], devoted literature on the application of mmWave automotive radars for the said application is unreported.

7.2. Traditional Use of ZFFT

Legacy use of ZFFT comprised the application of FFT to a specific portion of interest instead of the entire spectrum. The proceeding discussion is based on [55,56] coupled with the authors' comments. The FFT is an efficient implementation of the DFT as expressed in (2), with spectral resolution, Δf, given by

$$\Delta f = \frac{F_s}{N}, \tag{22}$$

where N is the order of the FFT and F_s is the sampling rate of ADC. From (22), it is evident that a larger N results in finer frequency resolution. Due to practical considerations, the radix-2 Cooley–Tukey implementation of the FFT is commonly used in DSPs. Its computational complexity involves $N\log_2(N)$ additions and $N/2\log_2(N)$ multiplications. Consequently, increasing N drastically increases the volume of required processing, making the approach unfeasible. Alternatively, reducing F_s achieves the same goal but leads to a loss of high-frequency components per the definition of the Nyquist sampling theorem [57]. Traditional implementation of ZFFT entails identifying a band of interest cascaded by a mixer to shift the band down to the DC component. Eventually, a low-pass filter is applied with decimation by a factor corresponding to the band of interest as a percentage of the entire spectrum. The process can be mathematically expressed as

$$x_D = \downarrow D\Big(LP(x_F.e^{-j2\pi F_c/F_s})\Big), \tag{23}$$

where x_D and x_F are the decimated and whole equivalents, respectively, in the spectral domain, while $\downarrow$ is the decimation operator and D is the decimation factor, expressed as

$$D = \frac{F_s}{F_c}, \tag{24}$$

where F_c is the center frequency of ROI, and LP is the low-pass filter used to suppress the high-frequency components resulting from complex multiplication in the mixing stage. The fundamental idea underlying ZFFT is to retain the same spectral resolution provided by a full-size FFT on the original time-domain signal while performing a smaller FFT on the decimated signal. Stated simply, a reduced sampling rate, F_s/D, and a shorter time-domain signal of length, N/D, uphold the spectral resolution while a drastic reduction in computational complexity by a factor, D, is achieved.

7.3. Enhancing Spectral Resolution with ZFFT

The objective of this effort is to improve accuracy in the range measurement, deviating from the commonly accepted definition of range resolution. A chirp with a high gradient and a longer duration is expected to provide better range resolution based on the characteristics of the Fourier transform. Nevertheless, the primary objective of a radar altimeter is not to distinguish closely positioned targets, but, rather, to calculate the distance from a single target, the surface of the ground. This transforms the need for precise measurement of distinct targets into the objective of enhancing the accuracy of range measurement for a

single target. Governed by the spectral resolution, a single target has the ability to generate a wide range of beat frequencies, rather than being limited to a discrete set of range bins. Accordingly, the spectral resolution can be enhanced by increasing the order of FFT to generate precise beat frequencies.

Due to the unavailability of data for fixed-wing UASs, the authors opted to analyze the scenario of a commercial aircraft. This decision is rooted in the goal of illustrating a proof of concept rather than using actual data. Table 8 includes operational requirements taken from an Airbus A350 aircraft, with appropriate safety margins [58]. The radar specifications are based on the manual of the breakout board, IWR1843BOOST. Together, these requirements establish the foundation for deriving waveform specifications summarized in Table 9. In the existing scenario, the SNR exceeds the minimum threshold recommended by the radar manufacturer, with a considerable margin [59]. The NRCS was chosen, with the runway considered as low-relief terrain. For readers interested in a deeper understanding of the selected model and NRCS estimation, it is recommended to consult reference clutter estimation models [51,60,61]. Given that the target is the smooth surface of the runway, the variation in the terrain has been ignored. Furthermore, since the SNR is considerably high as the maximum altitude requirement is only a couple of meters, there is no need to concatenate multiple chirps in the FMCW frame. Accordingly, the impact of V_{rad} due to ROD has been ignored as well.

Table 8. Operational requirements for the touchdown stage.

Requirement	Value	Remarks
R_{acc}	$\pm$1 mm	Range Accuracy
R_{min}	2 m	Minimum Altitude
R_{max}	4 m	Maximum Altitude
V_{lat}	20 m/s	Maximum Lateral Velocity
RoD	0 m/s	Maximum Rate of Descent
σ_h	0 m	Maximum Standard Deviation of Terrain
V_{rad}	0 m/s	Maximum Radial Velocity
SNR_{min}	20 dB	Minimum SNR Requirement
T	25 °C	Antenna Temperature

Table 9. Waveform specifications for the touchdown stage.

Parameter	Value	Remarks
Δt_{max}	12.22 ms	Max Time B/W Data Updates
U_{min}	82 Hz	Minimum Update Rate
T_c	102.4 µs	Chirp Duration
B	3.45 GHz	Chirp BW
$\Delta R(B)$	4.35 cm	The function of Chirp BW
IF_{max}	4.5 MHz	Maximum Beat Frequency for Max Range
F_s	5 MSPS	Sampling Rate in Mega Samples Per Second
S	33.69 MHz/µs	Chirp Slope
N_{coarse}	512	Coarse FFT Size
Δf	1.974 KHz	Frequency Resolution
$\Delta R(F_s, N_{FFT}, S)$	0.86 m	Function of Sampling Rate, FFT, and Slope
N_{Dopp}	1	Number of Chirps/Frame
T_F	102.4 µs	Frame Duration
N_{Tx}	1	Number of Transmit Antennae
N_{Rx}	1	Number of Receive Antennae
θ_{res}	N/A	Angular Resolution
B_n	5 KHz	Noise Bandwidth
P_n	$-$119.2 dBm	Noise Power
σ_0	2.47	NRCS
P_r	$-$60.47 dBm	Received Power at 4 m
SNR	58.75 dB	At 4 m AGL

The subsequent discourse delineates a systematic approach formulated to achieve accurate altitude estimation, accompanied by pertinent theoretical principles. Figure 16 depicts the sequence of actions involved in generating the fine beat frequency, culminating with altitude reporting at the last stage.

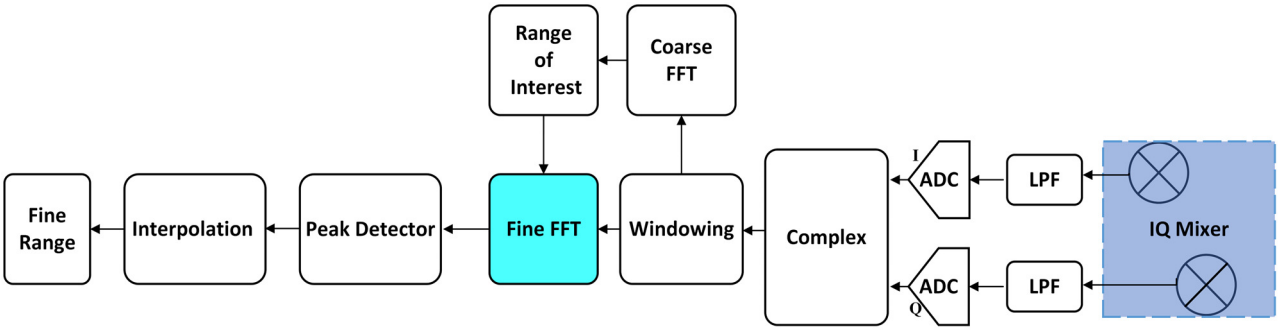

Figure 16. Zoom FFT implementation.

The time-domain I/Q components of the beat frequency are recorded in their respective ADC channels. The subsequent stage involves applying symmetric tapering through windowing. The selection of a window function is aimed at maintaining the integrity of the signal by keeping the core range bins unaltered while reducing the influence of chirp transitions. This mitigates spectral leakage and improves the precision of measurements. Unlike the typical ZFFT, an alternative approach involves striking a compromise between resource conservation and obtaining high precision.

The time-domain signal is initially subject to a coarse FFT of size N_1. Afterward, the range bin that has the highest peak along with neighboring bins on either side are identified as the region of interest. Choosing the size of this region depends on the spectral resolution provided by the coarse FFT and the geometry of the target. An object having an irregular surface is likely to be present in multiple range bins. A thoughtful selection of two adjacent range bins on either side for a smooth runway surface was made. Consequently, a small area of interest results in reduced computational complexity while maintaining the range accuracy. The objective is to calculate the beat frequency with extremely precise spectral resolution by performing a second stage of FFT with order N_2 on the region of interest identified in the previous step. The same time-domain signal utilized in the first step is once again utilized in the second stage. The mathematical expression for ZFFT can be given for each value of n_c ranging from $L \leq n_c \leq U$ as

$$X[k] = \sum_{n=0}^{N_1-1} x[n] e^{\frac{-j2\pi.n_c.n}{N_1}} e^{\frac{-j2\pi.n_f.n}{N_1.N_2}}, 0 \leq k \leq N_1 - 1, 0 \leq n_f \leq N_2 - 1, \quad (25)$$

where $X[k]$ is the spectral counterpart of the time-domain signal $x[n]$. L and U are the start and end range bin indices spanning the region of interest, while n_c and n_f are the coarse and fine range bin indices, respectively. Accordingly, N_1 and $N_1 \times N_2$ are the respective coarse and fine FFT orders in the two-stage process. Equation (25) appears daunting from a mathematical aspect and therefore warrants a simplified explanation. The entire operation is centered around the multiplication of the input signal using meticulously selected complex exponentials known as twiddle factors. These are commonly utilized in the majority of DSP implementations of FFT and recorded as preprogrammed values in a truth table. The crucial concept to grasp is the choice of the coarse and fine twiddle elements. Contrary to the use of index, k, in the twiddle factors of a conventional FFT, coarse range bin index is present in the coarse twiddle factor. As each coarse range bin corresponds to a distinct frequency component, multiplying it with the coarse twiddle factor determines the starting value of the ROI. Afterward, frequency values corresponding to the coarse range bins are further multiplied with fine twiddle factors as analyzing functions, making the spectral resolution equivalent to an FFT with order $N_1 \times N_2$. This approach produces

an increased spectral resolution as if an FFT with order $N_1 \times N_2$ was applied to the entire time-domain signal. Eventually, a significant reduction in computational resources is achieved while very high accuracy is achieved. In the preceding text, it was argued that a runway surface is anticipated to require a small region of interest in the coarse FFT stage. However, the distribution of the range profile into very fine range bins is likely to divide even a very smooth and flat target into multiple fine range bins. Aptly, an additional step of interpolation is performed. This serves as a correction to further improve the accuracy. The process comprises searching for a peak in the fine range profile and evaluating the weights of immediate neighboring bins. The fine range bin index, F, is expressed as

$$F = \text{argmax}_{0 \le i \le 5N_2}(a_i), \tag{26}$$

where a_i corresponds to the value in each fine range bin spanning from 0 to $5N_2$. Multiplication by 5 signifies the number of coarse range bins. The *argmax* function returns the index of the fine range bin containing the peak value. Subsequently, a correction factor as an interpolation index is added to the beat frequency resulting in an even finer position of the target. The interpolation index, I, is mathematically expressed as

$$I = \frac{p - n}{2(p + n - 2m)}, \tag{27}$$

where p and n are the values in the neighboring bins to the left and right, respectively, with reference to the fine range bin index having a peak value, m. The last stage comprises the estimation of fine beat frequency. Since the spectral resolution has been improved as a result of the ZFFT algorithm, (22) can now be rewritten as

$$\Delta f_{fine} = \frac{F_s}{N_1 N_2}. \tag{28}$$

Using the fine range bin index with peak value and interpolation index, the fine beat frequency can be estimated as

$$f_{fine} = \Delta f_{fine}(N_1 L + F + I). \tag{29}$$

Using (29), the fine range estimate, R_{fine}, can be evaluated as

$$R_{fine} = \frac{c f_{fine}}{2S}. \tag{30}$$

It is prudent to present a comparison of range accuracy for coarse and fine range profiles. FFT sizes, N_1 and N_2, are chosen as 512 each. The spectral resolution for the specific area of interest is determined by an FFT size of 512 × 512 (256 K). Figure 17a,b depict the coarse and fine range profiles, respectively. These profiles were obtained from a static experiment using the IWR1843BOOST platform, fixed on a tripod and positioned at a grazing angle of 90° against a concrete wall. The coarse FFT was performed on the DSP section of the radar chipset, and the resulting FFT data were then exported to a PC for post-processing in the second stage. Table 10 presents a concise overview of the findings with a precise range accuracy of 0.082 mm.

Table 10. Summary of results for the zoom FFT.

Parameter	Value	Remarks
N_1	512	Coarse FFT Size
C	32	Coarse Range Bin Index
L	30	ROI Start Index
N_{zoom}	5	Number of Range Bins in ROI
Δf_{coarse}	9.765 KHz	Coarse Spectral Resolution
ΔR_{coarse}	4.35 cm	Coarse Range Resolution

Table 10. *Cont.*

f_{coarse}	312.48 KHz	Coarse Beat Frequency
N_1N_2	262,144	Fine FFT size
R_{coarse}	1.3912 m	Coarse Range
Δf_{fine}	19.0735 Hz	Fine Spectral Resolution
ΔR_{fine}	0.082 mm	Fine Range Resolution
I	0.0180	Interpolation Index
F	1472	Fine Range Bin Index
f_{fine}	321.045 KHz	Fine Beat Frequency
R_{fine}	1.4290 m	Fine Range

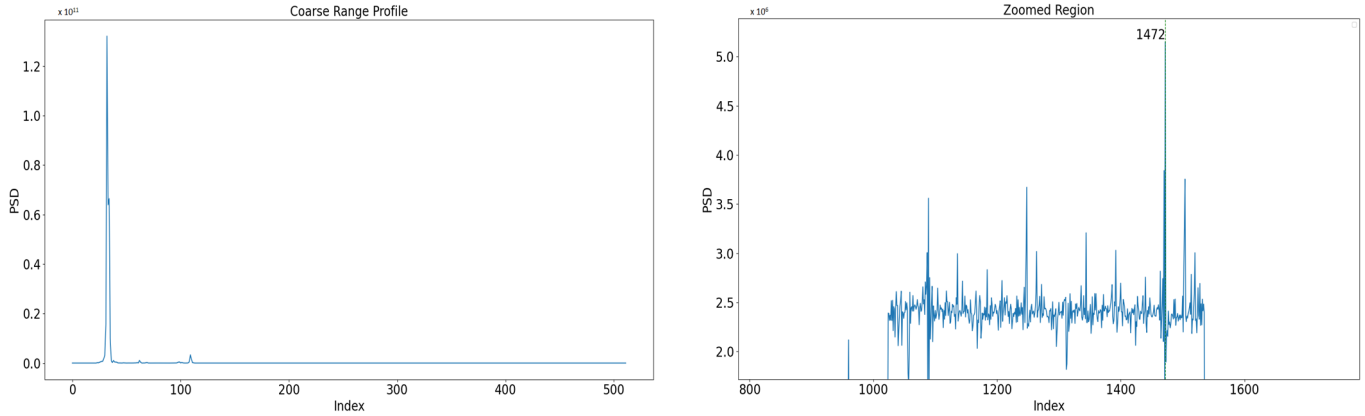

(**a**) (**b**)

Figure 17. Range profiles: (**a**) Coarse; (**b**) fine.

8. Discussion

Having established the foundation for migration to mmWave altimetry for UASs in the preliminary work, this article aims to advance the discussion by providing a signal processing framework. The article maintains a tutorial approach to engage a broad readers, ranging from application engineers to seasoned academicians.

The framework for developing a comprehensive mmWave altimetry solution for UASs using automotive radars is focused on overcoming inherent hardware limitations, including Tx power and IF filter bandwidth. Both the preliminary work and this article focus on optimizing performance metrics for each stage of flight within these hardware constraints. Tailoring these metrics to meet the requirements of an mmWave altimeter with a stage adaptive waveform benefits greatly from the software-defined architecture. The contribution of this body of work is the meticulous documentation of engineering involved in waveform design by prioritizing metrics according to their relevance in the respective stage of flight. Contrary to the concept of legacy RA, all nine performance metrics listed in Table 1 have been involved in the waveform design.

The signal processing aspects were elucidated, with each stage being simulated as a radar scenario. As highlighted in this study as well as the preliminary work, the intertwined nature of performance metrics requires careful consideration. For instance, the radial velocity component in the cruise stage does not have a significant impact as the target was empirically estimated to be always present in the 0th Doppler bin. However, it was observed that the target migrates to neighboring range bins due to the motion of the platform relative to the ground surface. Despite the radial velocity component arising from variations in the terrain profile and a chirp with a very long duration, the resultant range accuracy remained within the limits specified by operational requirements.

A novel contribution of this work was proposing TDM-MIMO for maximizing angular resolution as long as ROD remains within the $V_{\max}$ limit in the landing approach stage. Owing to the relatively relaxed maximum range requirement, the chirp duration

was reduced to cater to the maximum ROD. Fundamental concepts involved in Doppler compensation for a TDM-MIMO radar were presented mathematically for resolving phase ambiguity due to simultaneous motion and off-boresight angular position of the target. Lastly, in the touchdown stage, range accuracy was prioritized above all in the waveform design process since $V_{\max}$, AoA, and maximum range were largely irrelevant.

For the detection methodology, the suitability of three CFAR variants was appraised, with CFAR-CASO offering a reasonable compromise over others in the cruise and landing approach stage. The touchdown stage does not warrant CFAR detection owing to the straightforward characteristics of the runway. The underpinnings of CFAR, associated signal processing aspects, and the flow of operations were covered in reasonable detail from a mathematical standpoint.

8.1. Challenges

Having covered mmWave altimetry for UASs in great detail with supporting arguments, mathematical illustrations, and insights, it is now imperative to lay the groundwork for the culmination of the work. It is envisioned that the framework for deriving waveform specifications from operational requirements and simulation results must be validated in a real-world scenario. A two-stage approach for the execution of this yearning is to simulate a radar scenario with the target being the ground surface using the DTED of an actual runway. In the existing study, the targets were treated as uniform bodies, and a free space propagation model was employed. However, the true emulation of an actual scenario must consider the effect of specular reflections from the ground terrain. Afterward, it is planned to mount the radar on a small-sized drone and emulate all three stages of flight. Furthermore, a complete simulation of the landing scenario is planned using clutter generated from the actual DTED of runway surroundings. The advantage of employing TDM-MIMO in the determination of actual altitude, as opposed to a traditional RA, shall also be investigated in the upcoming research phase. This direction has groundbreaking potential to improve landing safety and maintain constant altitude in surveillance operations. The promising simulation results and alignment with practical operational requirements demonstrate the viability of mmWave altimetry using automotive radars, achieved through the optimization of performance metrics. Given the growing applications of UASs in modern life, the potential of mmWave altimetry for UASs warrants a dedicated MOPS tailored to specific operational needs.

8.2. Future Work

Despite promising outcomes, there are inherent obstacles to the pursuit of future goals. Firstly, the simulation scenarios covered in this work must be implemented on actual hardware. The zoomed-in range profile using the ZFFT algorithm illustrated in Section 7 was generated using actual hardware, but the update rate was not part of the equation. During the touchdown estimation stage, the update rate is equally as critical as the range accuracy. The real-time reporting of altitude to FCC is necessary to engage subsequent control actions. Similarly, there is a need to implement requisite waveforms for all three flight stages. It is safe to assume that the cruise and landing approach entail relatively slow update rates and the real challenge resides in the touchdown stage. Accordingly, documenting the implementation details and the characterization of performance profiles comprising range accuracy and processing latency is mandatory. Another daunting challenge is managing the seamless transition between flight stages or, in other words, the engineering design of the hysteresis loop [62]. The constant switching between waveform configurations at the borderline of altitude limits must be handled gracefully. An important goal from a systems engineering view is to ensure that failures and abnormal limits are well catered for at all times. One particular scenario that requires careful consideration is the drone exceeding the maximum limit of ROD in the landing approach stage. Consequently, Doppler compensation shall not be performed correctly, resulting in erroneous AoA. For a safety-critical application such as an emergency landing, this could lead to a catastrophic

outcome if the landing relies solely on a single radar sensor. It is crucial to guarantee accurate reporting or no reporting at all, without any possibility of incorrect readings. One potential way out is to extend the V_{max} and resort to methods aimed at resolving the velocity ambiguity, employing methodology cited in a related dissertation [63]. However, in the existing scope, there is a limit to extending the V_{max}, and a scenario of V_{max} being exceeded may arise regardless. In this context, a consolidated solution is mandatory that outlines the direction for future research. Lastly, it is envisioned that the summary of cited challenges, proposed solutions, and succinct details entailing this endeavor and preliminary work culminating into clutter simulation and experimental validation shall be documented in a comprehensive letter.

9. Conclusions

This paper provides a signal processing framework for an adaptive mmWave RA intended for three phases of the UAS flight, providing a follow-up to the authors' earlier work. This article provides a methodology for improving capabilities by utilizing the previously unexplored idea of AoA estimation for RAs of UASs. Moreover, it argues the potential of mmWave altimetry as a software redundancy for WoW systems in UASs. This paper covers chirp integration, range-Doppler maps in radar cubes, and the selection of optimal windowing method from a practical perspective. For each stage of flight, the rationale for prioritizing performance metrics amidst accompanying intricacies in the waveform design process was offered with insightful discussions. For the cruise stage, the waveform was designed to enhance maximum altitude while upholding high-range resolution while considering the effects of terrain elevation. The use of TDM-MIMO for AoA estimation in the landing approach stage and ZFFT for mm-level range accuracy in the touchdown stage of UAS flight were previously unreported in the literature. The text explores all cited aspects through a signal-processing lens, following a structured flow to achieve the end goal amidst challenges and limitations intrinsic to automotive radars. Each stage of the flight was simulated as an FMCW radar scenario coupled with mathematical expressions to consolidate the discussion. CFAR detection algorithm along with its variants were appraised in a simulation environment, with CFAR-CASO offering a convenient balance for the cruise and landing approach stage. Afterwards, a succinct discussion was presented to coalesce the insights offered by the extensive body of work. Lastly, the inherent challenges and potential directions for future research were submitted.

Author Contributions: Investigation, resources, visualization, writing—original draft preparation, software: M.A.A.; Conceptualization, methodology: M.A.A. and Y.D.; validation, supervision, writing—review and editing: Y.D., M.D. and A.K. All authors have read and agreed to the published version of the manuscript.

Funding: This research received no external funding.

Data Availability Statement: The simulation environment, scripts, and dataset generated and/or characterized during this study are available from the corresponding author upon reasonable request.

Conflicts of Interest: The authors declare no conflicts of interest.

List of Abbreviations

Abbreviation	Definition
EM	Electromagnetic
UAS	Unmanned aerial system
FMCW	Frequency modulated continuous wave
nm	nanometer
RFFE	Radio frequency front end
5G	Fifth-generation
RA	Radar altimeter
GHz	Gigahertz

MOPS	Minimum operational performance standards
SWaP	Size, weight, and power
AGL	Above ground level
Tx	Transmit
Rx	Receive
HPBW	Half-power beam-width
AoA	Angle of arrival
VTOL	Vertical take-off and landing
WoW	Weight-on-wheels
FCC	Flight control computer
mm	Millimeter
LoS	Line of sight
ADC	Analog-to-digital converter
CFAR	Constant false alarm rate
ZFFT	Zoom fast Fourier transform
TDM-MIMO	Time-division multiplexing multiple input–multiple output
FOV	Field of view
ROD	Rate of descent
ROI	Region of interest
IRA	Interferometric radar altimeter
TRN	Terrain-referenced navigation
GPS	Global Positioning System
DC	Direct current
SDK	Software Development Kit
BW	Bandwidth
3D	Three-dimensional
SNR	Signal-to-noise ratio
FFT	Fast Fourier transform
LFM	Linear frequency modulation
DSP	Digital signal processor
PRI	Pulse repetition interval
FIR	Finite impulse response
DFT	Discrete Fourier transform
PFA	Probability of false alarm
SIMO	Single input multiple output
CFAR-CA	CFAR cell averaging
CFAR-CASO	CFAR cell averaging smallest of
CFAR-CAGO	CFAR cell averaging greatest of
LNA	Low noise amplifier
TDM	Time-division multiplexing
BPM	Binary phase modulation
BPM-MIMO	Binary phase modulation multiple input–multiple output
RCS	Radar cross-section
TSC	Technology Service Corporation
NRCS	Normalized radar cross-section
APL	Applied Physics Laboratory
I/Q	In-phase and quadrature
DTED	Digital terrain elevation data

References

1. Nebylov, A. Radar Altimeters. In *Aerospace Sensors*, 1st ed.; Momentum Press: New York, NY, USA, 2012; pp. 55–88.
2. Pulutan, D.K.A.; Marciano, J.S. Design Trade-Offs in a Combined FMCW and Pulse Doppler Radar Front-End. In Proceedings of the IEEE 2013 Tencon—Spring, Sydney, Australia, 17–19 April 2013; IEEE: Piscataway, NJ, USA, 2013; pp. 567–571. [CrossRef]
3. Richards, M.A.; Scheer, J.A.; Holm, W.A. (Eds.) *Principles of Modern Radar: Basic Principles*; Scitech Publishing: Raleigh, NC, USA, 2010; ISBN 9781891121524.
4. Canada, T.J. Handbook on Radio Frequency Spectrum Requirements for Civil Aviation Part I. In Proceedings of the 28th Meeting of Working Group F Aeronautical Communications Panel, Lima, Peru, 11–22 March 2013.

5. Awan, M.A.; Dalveren, Y.; Kara, A.; Derawi, M. Towards mmWave Altimetry for UAS: Exploring the Potential of 77 GHz Automotive Radars. *Drones* **2024**, *8*, 94. [CrossRef]
6. EUROCAE. *Minimum Performance Specification for Airborne Low Range Radio Altimeter Equipment*; ED-30; EUROCAE: Saint-Denis, France, 1980.
7. RTCA. *Minimum Performance Standard for Airborne Low-Range Radar Altimeters*; DO-155; RTCA: Washington, DC, USA, 1974.
8. LR-D1 Pro: Dual-Band Radar Altimeter. Available online: https://ainstein.ai/lr-d1-pro-dual-band-radar-altimeter/ (accessed on 7 June 2024).
9. Honeywell. ALA-52B Radio Altimeter. Available online: https://aerospace.honeywell.com/us/en/products-and-services/product/hardware-and-systems/navigation-and-radios/ala-52b-radar-altimeter (accessed on 22 June 2024).
10. Drone Technology in Agriculture. Available online: https://www.croptracker.com/blog/drone-technology-in-agriculture.html (accessed on 16 June 2024).
11. Finklea, K. Law Enforcement and Technology: Use of Unmanned Aircraft Systems. Available online: https://crsreports.congress.gov/product/pdf/R/R47660 (accessed on 15 June 2024).
12. Nguyen, D.D.; Rohacs, J.; Rohacs, D. Autonomous Flight Trajectory Control System for Drones in Smart City Traffic Management. *ISPRS Int. J. Geo-Inf.* **2021**, *10*, 338. [CrossRef]
13. Ha, J.-S.; Hong, S.-Y. Altimetry Method for an Interferometric Radar Altimeter Based on a Phase Quality Evaluation. *Sensors* **2023**, *23*, 5508. [CrossRef] [PubMed]
14. Brindisi, A.; Vendittozzi, C.; Travascio, L.; Di Palma, L.; Belardo, M.; Ignarra, M.; Fiorillo, V.; Concilio, A. Preliminary Assessment of an FBG-Based Landing Gear Weight on Wheel System. *Actuators* **2022**, *11*, 191. [CrossRef]
15. MathWorks. Radar Toolbox. Available online: https://www.mathworks.com/help/radar/ (accessed on 24 March 2024).
16. Texas Instruments. IWR1843BOOST Evaluation Module for Single Chip 77 GHz mmWave Sensor. Available online: https://www.ti.com/tool/IWR1843BOOST (accessed on 14 April 2024).
17. Zhang, Y.; Qiao, Y.; Li, G.; Li, W.; Tian, Q. Random Time Division Multiplexing Based MIMO Radar Processing with Tensor Completion Approach. *Sensors* **2023**, *23*, 4756. [CrossRef] [PubMed]
18. MathWorks. Radar Data Cube. Available online: https://www.mathworks.com/help/phased/gs/radar-data-cube.html (accessed on 11 May 2024).
19. Frick, S. Radar Altimeters: Overview of Operation, Design, and Performance. Available online: https://avsi.aero/wp-content/uploads/2021/12/Radar-Altimeter-Overview-of-Design-and-Performance.pdf (accessed on 19 April 2024).
20. Cai, L.; Ma, X.; Xu, Q.; Li, B.; Ren, S. Performance Analysis of Some New CFAR Detectors under Clutter. *J. Comput.* **2011**, *6*, 1278–1285. [CrossRef]
21. Texas Instruments. *High Accuracy Range Measurement–16xx*; Texas Instruments: Dallas, TX, USA, 2017.
22. Nam, S.H.; Sung, C.K.; Lee, S.W., 3rd. Order RB-PMF based Terrain Aided Navigation Algorithm considering Altitude Error. In Proceedings of the Korean Society for Aeronautical and Space Sciences Fall Conference, Jeju, Republic of Korea, 28 November–1 December 2018; pp. 291–292.
23. Sung, C.K.; Lee, S.J. Performance Comparisons of Terrain Referenced Navigations Based on PMF and RB-PMF Considering Altitude Error. In Proceedings of the Korean Society for Aeronautical and Space Sciences Fall Conference, Jeju, Republic of Korea, 28 November–1 December 2018; pp. 974–975.
24. Robey, F.C.; Coutts, S.; Weikle, D.; McHarg, J.C.; Cuomo, K. MIMO Radar Theory and Experimental Results. In Proceedings of the Conference Record of the Thirty-Eighth Asilomar Conference on Signals, Systems and Computers, Pacific Grove, CA, USA, 7–10 November 2004; IEEE: Piscataway, NJ, USA, 2004; pp. 300–304.
25. Patole, S.M.; Torlak, M.; Wang, D.; Ali, M. Automotive Radars: A Review of Signal Processing Techniques. *IEEE Signal Process. Mag.* **2017**, *34*, 22–35. [CrossRef]
26. Rao, S. "MIMO Radar." Texas Instruments, Dallas, TX, USA, Appl. Rep. SWRA554A, Jul. 2018. Available online: https://www.ti.com/lit/an/swra554a/swra554a.pdf (accessed on 5 April 2024).
27. Li, X.; Wang, X.; Yang, Q.; Fu, S. Signal Processing for TDM MIMO FMCW Millimeter-Wave Radar Sensors. *IEEE Access* **2021**, *9*, 167959–167971. [CrossRef]
28. Rohling, H.; Mende, R. OS CFAR performance in a 77 GHz radar sensor for car application. In Proceedings of the International Radar Conference, Beijing, China, 8–10 October 1996; pp. 109–114.
29. Hugler, P.; Geiger, M.; Waldschmidt, C. 77 GHz Radar-Based Altimeter for Unmanned Aerial Vehicles. In Proceedings of the 2018 IEEE Radio and Wireless Symposium (RWS), Anaheim, CA, USA, 15–18 January 2018; IEEE: Piscataway, NJ, USA, 2018; pp. 129–132.
30. Hugler, P.; Roos, F.; Schartel, M.; Geiger, M.; Waldschmidt, C. Radar Taking Off: New Capabilities for UAVs. *IEEE Microw. Mag.* **2018**, *19*, 43–53. [CrossRef]
31. Başpınar, Ö.O.; Omuz, B.; Öncü, A. Detection of the Altitude and On-the-Ground Objects Using 77-GHz FMCW Radar Onboard Small Drones. *Drones* **2023**, *7*, 86. [CrossRef]
32. Ma, J.; Xiang, J.; Peng, F. Performance Analysis of CFAR Detector Based on Censored Mean and Cell Average. *J. Phys. Conf. Ser.* **2019**, *1237*, 022029. [CrossRef]
33. Lyons, R.G. *Understanding Digital Signal Processing*, 3rd ed.; Prentice Hall: Upper Saddle River, NJ, USA, 2011.
34. Sakhuja, N. *MMWAVE-SDK Deep Dive*; Texas Instruments: Dallas, TX, USA, 2020.

35. MathWorks. Phased Array System Toolbox. Available online: https://www.mathworks.com/help/phased (accessed on 15 May 2024).
36. van de Zande, I.G. 3D Point Cloud Object Detection for Millimeter Wave Radar: A Synthesis Study. Master's Thesis, University of Twente, Enschede, The Netherlands, September 2023.
37. Dham, V. Programming Chirp Parameters in TI Radar Devices. Texas Instruments, Dallas, TX, USA, Appl. Rep. SWRA553A, Feb. 2020. Available online: https://www.ti.com/lit/an/swra553a/swra553a.pdf (accessed on 4 May 2024).
38. Rao, S.; Nayyar, J.; Yan, M.; Johnson, B. *Introduction to the DSP Subsystem in the AWR16xx, May 2017*; Texas Instruments: Dallas, TX, USA, 2017.
39. Chaudhari, Q. FMCW Radar Part 2—Velocity, Angle and Radar Data Cube. Available online: https://wirelesspi.com/fmcw-radar-part-2-velocity-angle-and-radar-data-cube/ (accessed on 5 April 2024).
40. National Instruments. Understanding FFTs and Windowing. Available online: https://download.ni.com/evaluation/pxi/Understanding%20FFTs%20and%20Windowing.pdf (accessed on 12 May 2024).
41. Oppenheim, A.V.; Schafer, R.W. *Discrete-Time Signal Processing*, 2nd ed.; Prentice Hall: Upper Saddle River, NJ, USA, 1999.
42. Mahafza, B.R. *Radar Systems Analysis and Design Using MATLAB*, 3rd ed.; CRC Press: Boca Raton, FL, USA, 2013.
43. Rao, S. Introduction to mmwave Sensing: FMCW Radars. Available online: https://e2e.ti.com/cfs-file/__key/communityserver-discussions-components-files/1023/Introduction-to-mmwave-Sensing-FMCW--Radars.pdf (accessed on 26 March 2024).
44. Skybrary. Cruise. Available online: https://skybrary.aero/cruise (accessed on 17 March 2024).
45. National Oceanic and Atmospheric Administration. Radar Images: Velocity. Available online: https://www.noaa.gov/jetstream/velocity (accessed on 2 June 2024).
46. MathWorks. Reflectivity of Land Surface. Available online: https://www.mathworks.com/help/radar/ref/landreflectivity.html (accessed on 27 March 2024).
47. MathWorks. Constant False Alarm Rate (CFAR) Detection. Available online: https://www.mathworks.com/help/phased/ug/constant-false-alarm-rate-cfar-detection.html (accessed on 9 May 2024).
48. DJI. Matrice 30 Series, Specifications. Available online: https://enterprise.dji.com/matrice-30/specs (accessed on 11 May 2024).
49. U.S. Department of Transportation, Federal Aviation Administration. Approaches and Landings. In *Airplane Flying Handbook*; U.S. Department of Transportation, Federal Aviation Administration: Oklahoma City, OK, USA, 2021; ISBN 979-8776143243.
50. MathWorks. Normalized sea surface reflectivity. Available online: https://www.mathworks.com/help/radar/ref/seareflectivity.html (accessed on 12 May 2024).
51. Reilly, J.P.; McDonald, R.L.; Dockery, G.D. *RF-Environment Models for the ADSAM Program*; Report No. A1A97U 070; Johns Hopkins University Applied Physics Laboratory: Laurel, MD, USA, 1997. Available online: https://apps.dtic.mil/sti/citations/ADA346190 (accessed on 13 April 2024).
52. Toa, M.; Whitehead, A. *Ultrasonic Sensing Basics*; Texas Instruments: Dallas, TX, USA, 2019.
53. Vargas, J.; Alsweiss, S.; Toker, O.; Razdan, R.; Santos, J. An Overview of Autonomous Vehicles Sensors and Their Vulnerability to Weather Conditions. *Sensors* **2021**, *21*, 5397. [CrossRef] [PubMed]
54. Soares, P.F.M. Flight Data Monitoring and its Application on Algorithms for Precursor Detection. Master's Thesis, Instituto Superior Técnico, Lisboa, Portugal, November 2014.
55. Al-Qudsi, B.; Joram, N.; Strobel, A.; Ellinger, F. Zoom FFT for Precise Spectrum Calculation in FMCW Radar Using FPGA. In Proceedings of the Proceedings of the 2013 9th Conference on Ph.D. Research in Microelectronics and Electronics (PRIME), Villach, Austria, 24–27 June 2013; IEEE: Piscataway, NJ, USA, 2013; pp. 337–340.
56. MathWorks. Zoom FFT. Available online: https://www.mathworks.com/help/dsp/ug/zoom-fft.html (accessed on 18 May 2024).
57. Shannon, C.E. Communication in the Presence of Noise. *Proc. IRE* **1949**, *37*, 10–21. [CrossRef]
58. Airbus, S.A.S. *Airbus A350: Aircraft Characteristics, Airport and Maintenance Planning*; Customer Services, Technical Data Support and Services: Blagnac, France, 2005.
59. Iovescu, C.; Rao, S. *The Fundamentals of Millimeter Wave Sensors*; White Paper SPYY005A; Texas Instruments: Dallas, TX, USA, 2016.
60. Ulaby, F.; Dobson, M.C.; Álvarez-Pérez, J.L. *Handbook of Radar Scattering Statistics for Terrain*; Artech House: Miami, FL, USA, 2019.
61. Long, M.W. *Radar Reflectivity of Land and Sea*, 3rd ed.; Artech House: London, UK, 2001.
62. Hysteresis in Digital Control Systems. Available online: https://www.hwe.design/theories-concepts/hysteresis (accessed on 20 June 2024).
63. Ahmed, B. Exploring the Potentials of Commercial Radar Chipsets for Proximity Sensing with Resolving Velocity Ambiguity. Ph.D. Thesis, Atilim University, Ankara, Turkey, 2022.